3-2005

An Examination of Range and Doppler Mismatch and their Effects on Radar Modeling

Gregory L. Izdepski

An Examination of Range and Doppler Mismatch and their Effects on Radar Modeling

THESIS

Gregory L. Izdepski, Captain, USAF

AFIT/GE/ENG/05-07

DEPARTMENT OF THE AIR FORCE
AIR UNIVERSITY

AIR FORCE INSTITUTE OF TECHNOLOGY

Wright-Patterson Air Force Base, Ohio

The views expressed in this thesis are those of the author and do not reflect the official policy or position of the United States Air Force, Department of Defense, or U.S. Government.

AFIT/GE/ENG/05-07

An Examination of Range and Doppler Mismatch and their Effects on Radar Modeling

THESIS

Presented to the Faculty

Department of Electrical and Computer Engineering

Graduate School of Engineering and Management

Air Force Institute of Technology

Air University

Air Education and Training Command

In Partial Fulfillment of the Requirements for the

Degree of Master of Science in Electrical Engineering

Gregory L. Izdepski, B.S.E.E.

Captain, USAF

March 2005

AFIT/GE/ENG/05-07

An Examination of Range and Doppler Mismatch and their Effects on Radar Modeling

Gregory L. Izdepski, B.S.E.E.
Captain, USAF

Approved:

/signed/	11 Mar 2005
Maj Todd B. Hale, PhD (Chairman)	date
/signed/	11 Mar 2005
Dr. Micheal A. Temple (Member)	date
/signed/	11 Mar 2005
Dr. Robert F. Mills (Member)	date

AFIT/GE/ENG/05-07

Abstract

A commonly accepted airborne phased array radar model simplifies the analytical derivation by assuming a waveform is perfectly matched in range and Doppler shift. This assumption means the matched filter output is effectively constant for all possible received scatterer Doppler and range mismatches, greatly simplifying the analytical development from that point forward. This research removes the matched Doppler and range assumption and examines the effects of several common waveforms on the model's fidelity along with the associated impact on radar performance, both non-adaptive and adaptive. Analysis is completed using power spectral density comparisons and the fully adaptive output signal to interference plus noise ratio comparison. Results indicate that the model's fidelity is impacted little by the Time Frequency Auto Correlation Function. However, change in bandwidth from the compressed waveforms does impact the model. Increased bandwidth introduces more thermal noise which dominates clutter returns. Therefore, the clutter problem becomes less difficult. The trade-off is a reduction in the resolution capability of the clutter spectrum.

Acknowledgements

First and foremost, I would like to express my sincere appreciation to my thesis advisor, Maj Todd Hale, PhD, for his guidance and support throughout the course of this research effort. His insight and knowledge that he imparted on me is very much appreciated. I would also like to thank my committee members Dr. Michael Temple and Dr. Robert Mills for their time, effort and willingness to help guide me in completing this research. In addition, I would like to thank my sponsors from the Air Force Research Laboratory Sensors Directorate, AFRL/SNRT, for both the support and latitude provided to me in this endeavor.

Special thanks go to my mother and sister for their constant encouragement and support through all phases of this research product.

I would especially like to thank my wife and children for their encouragement during the entire process. Their patience and understanding provided a supportive working environment at home.

Gregory L. Izdepski

Table of Contents

Page

List of Figures

List of Symbols

Symbol		Page
ϑ_x	Steering Variable in $\hat{x}$ Direction	10
ϑ_z	Steering Variable in $\hat{z}$ Direction	10
a_r	Received Signal Amplitude	10
f_o	Transmit Frequency	10
χ	Matched Filter of Received Signal	12
$h(t)$	Matched Filter Impulse Response	12
Φ	Time Frequency Auto Correlation Function	13
β	Dummy Variable for Integration	13
H	Hermitian	15
$\mathbf{a}(\vartheta_x)$	Azimuth Steering Vector	16
$\mathbf{e}(\vartheta_z)$	Elevation Steering Vector	16
$\mathbf{b}(\bar{\omega})$	Doppler Steering Vector	16
$\mathbf{v}$	Steering Vector	16
$f(\theta, \phi)$	Voltage Element Pattern	16
$g(\theta, \phi)$	Power Element Pattern	16
b_e	Backlobe Attenuation	17
$W(\theta, \phi)$	Weight Array Factor	18
σ^2	Johnson Noise	20
N_o	Noise Power Spectral Density	20
k	Boltzman's Constant	20
T_o	Standard Temperature	20
$\mathbf{R}_n$	Noise Covariance Matrix	20
$\mathbf{I}_{MNP}$	Identity Matrix	21
N_c	Number of Clutter Patches	21
θ_c	Elevation Angle for Clutter	21
R_c	Range to Clutter Patch	21
h_a	Aircraft Height	21

Symbol		Page
a_e	Effective Radius	21
N_r	Number of Rings	22
α_{il}	Random Clutter Patch Amplitude	23
σ_{il}	RCS of Clutter Patch	23
$\sigma_o(\theta_i, \phi_l)$	Ground Reflectivity	23
R_i	Range Ring	23
$\Delta\phi$	Angular Deviation	23
ΔR	Range Resolution	23
P_t	Power Transmitted	23
L_s	Power Loss	23
λ	Wavelength	23
$G_t(\theta_i, \phi_l)$	Array Pattern	23
$g(\theta_i, \phi_l)$	Element Pattern	23
T_c	Chip Width	25
Q	Number of Chips per Pulse	25
α	Chirp Rate	37
y	Number of Returned LFM Pulse	37

List of Abbreviations

Abbreviation		Page
TFACF	Time Frequency Auto Correlation Function	1
SNR	Signal-to-Noise Ratio	2
PSD	Power Spectral Density	2
SINR	Signal to Interference pulse Noise Ratio	2
PRI	Pulse Repetition Interval	6
PRF	Pulse Repetition Frequency	8
MF	Matched Filter	12
CNR	Clutter to Noise Ratio	23
AF	Ambiguity Function	25
LFM	Linear Frequency Modulation	37
SM	Signal Match	45
MV	Minimum Variance	45
MEM	Maximum Entropy Method	45
STAP	Space Time Adaptive Processing	50

An Examination of Range and Doppler Mismatch and their Effects on Radar Modeling

I. Introduction

Radar models and simulations provide insight into the operation of radar in real world conditions. A robust simulation is created by generating a complete radar model. The complete radar model includes accurately representing the physical radar with realistic operating parameters and environment characteristics.

Assumptions are a tool used in many models and simulations to simplify difficult problems. When creating the basic radar model, outlined later, assumptions are made to simplify the mathematics and simulations. The majority of these assumptions are valid under normal operating circumstances and have no adverse effects on simulation results when compared to real world operations.

There are two assumptions in focus throughout this research. The assumptions are that there is no mismatch in range and that a Doppler tolerant waveform is transmitted, even if the actual waveform is not Doppler tolerant. This research explores the removal of these assumptions and analyzes the effects of Doppler and range mismatch on the radar model.

1.1 Background

The first step to examining this issue is creating a radar model, commonly accepted by many in the Space Time Adaptive Processing community, for comparison. This model incorporates a Time Frequency Auto Correlation Function (TFACF) of the waveform, a formed antenna beam, beam steering abilities, and any effects from

thermal noise as well as clutter returns. The TFACF is where the assumptions are made.

The next step is to mathematically derive the TFACF expression for the non-Doppler tolerant waveform. The TFACF takes into account possible shifts within the matched filter due to Doppler and range cell mismatch. A limitation of no more than plus or minus a half chip width shift is placed on the derivation. This limitation allows the target Signal-to-Noise Ratio (SNR) to remain constant. A new weighted TFACF expression fits into the regular radar model at the same location as the Doppler tolerant expression of the TFACF.

Using the TFACF expression, simulations are run for several common waveforms. These waveforms are simulated using both radar models; the commonly accepted radar model (Space Time Adaptive Processing community) which assumes Doppler tolerance and perfect range matching, and the modified radar model which implements the TFACF allowing for Doppler and range mismatching. Results from each model are compared against each other using Power Spectral Density (PSD) methods as well as the fully adaptive radar processor Signal to Interference plus Noise Ratio (SINR) method. Analyzing the results, conclusions are drawn as to whether or not these effects are necessary for future modeling.

1.2 Organization

In chapter two, the commonly accepted radar model is outlined showing the development of the model including aperture geometries, transmitting/receiving signals, steering vector roles, and the environment characteristics. Within this development, the assumptions under question are highlighted. Then, in chapter three, the TFACF expression that accounts for Doppler and range shifting is found as well as how they relate with in the radar model. Chapter four shows the results and provides insight and analysis on how the two radar models differ. A summary of the entire research is covered in chapter five.

II. Literature Review

A complete understanding of the radar model is needed before addressing any effects that Doppler and range mismatching creates. This chapter outlines each separate segment that encompasses the radar model, along with signal processing techniques and overall system assumptions.

The radar model has been developed and modified throughout the years. This development of the radar model presented in this chapter is based on previous work [1, 5, 7] and written in this authors own words. The radar being simulated is based on an airborne phased array, pulsed Doppler system illuminating a target point scatterer. Therefore, all characteristics and properties of a pulse Doppler system are accounted for in the model.

Combining many different aspects together creates the radar model. The first aspect is to understand the geometry of the aperture. The geometry effects the antenna transmit pattern which is necessary for the radar range equation. The next step is to examine the transmit signal. After the transmit signal is reflected from a point scatter, the received signal is examined and processing occurs. A by-product of this processing is the steering vector. This steering vector allows for weighting on the antenna beam to allow for steering the beam in space and time. The next section of the model is builds the clutter and noise environment. However, before building the noise and clutter section of the model, the element and array pattern is needed. These patterns are needed because the clutter model is dependant on the radar equation which includes the antenna array and element patterns. At this point, the model is almost complete. The last two sections of the radar model include interferers with the received signal. Thermal noise occurs within each element in the array and needs to be accounted for and modeled. The last interferer is ground clutter.

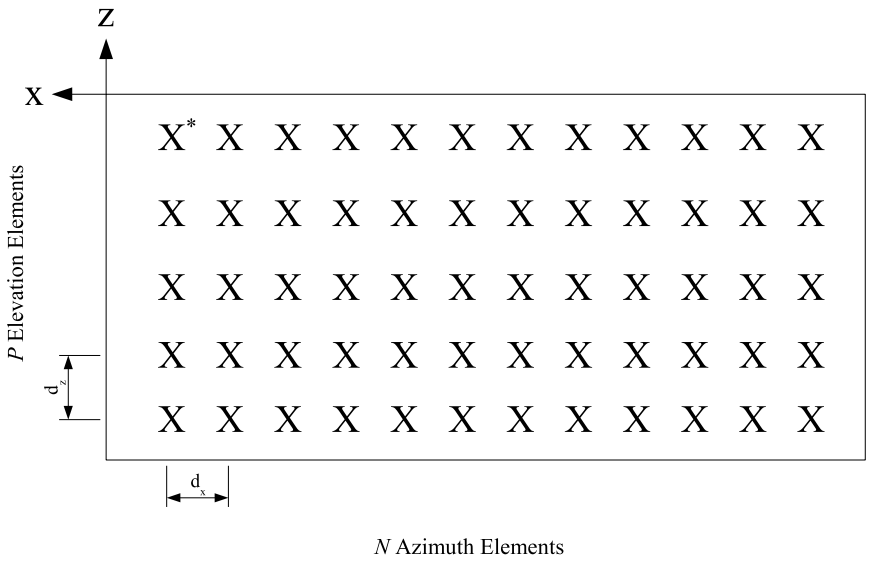

Figure 2.1: This shows the array configuration. Antenna elements are placed in the $\hat{x}$ and $\hat{z}$ direction with element spacing of d_x and d_z. Element X^* is located at $(x, z) = (0, 0)$.

2.1 Aperture Geometries

The aperture structure is the first block to be examined in the model. Understanding the geometry is necessary for development later in the model. Element and array patterns along with the steering vector are directly dependant on the set-up of the aperture geometry.

The antenna array structure consists of elements with the capacity of transmitting and receiving. Elements placed along the x-axis as well as the z-axis create a rectangular array. Each element is uniformly spaced at intervals of d_x and d_z. However, d_x and d_z are not necessarily equal. Notational wise, there are N d_x elements in the $\hat{x}$-direction (azimuth elements) and P represents elements in the $\hat{z}$-direction (elevation elements). Figure 2.1 shows the geometry of the array.

A generic expression describing the location of the np^{th} element is given by

$$d_{np} = -nd_x\hat{x} - pd_z\hat{z}, \tag{2.1}$$

where n ranges from 0 to $N-1$, p ranges from 0 to $P-1$, and $\hat{x}$ and $\hat{z}$ are unit vectors along the x-and z-axis, respectively.

The radar coordinate system uses θ to describe elevation and ϕ as azimuth. The reference element is the upper left of the array (annotated in Fig 2.1 by X^*). Thus, θ is negative when measured from bore sight toward the ground. Also, by placing the reference element at this position, d_{np} becomes negative in both the x and z-direction. Conversion from the radar coordinate system to the Cartesian coordinate system (needed later for the antenna array) is given by

$$\hat{k}(\theta,\phi) = \cos\theta\sin\phi\hat{x} + \cos\theta\cos\phi\hat{y} + \sin\theta\hat{z}. \tag{2.2}$$

The unit vector $\hat{k}$ is a reference vector in the direction of the target described by θ and ϕ, yet expressed in Cartesian coordinates.

Establishing the aperture geometry allows for continuing development with the rest of the model. In order for a radar to be able to detect targets in space, the radar must first transmit a signal. Therefore, an examination of the transmit signal is needed.

2.2 Transmit Signal

The radar transmit signal, labeled 'A' in Fig. 2.2, is a sinusoidal waveform, mathematically expressed as

$$s(t) = a_t u(t) e^{j(\omega_o t + \psi)}, \tag{2.3}$$

where a_t is the transmitted pulse amplitude and $u(t)$ is the envelope. The complex exponential describes the carrier frequency ω_o and the random phase shift ψ. The random phase shift is necessary since the phase state of the transmitted cosine waveform is not known at the time of transmission.

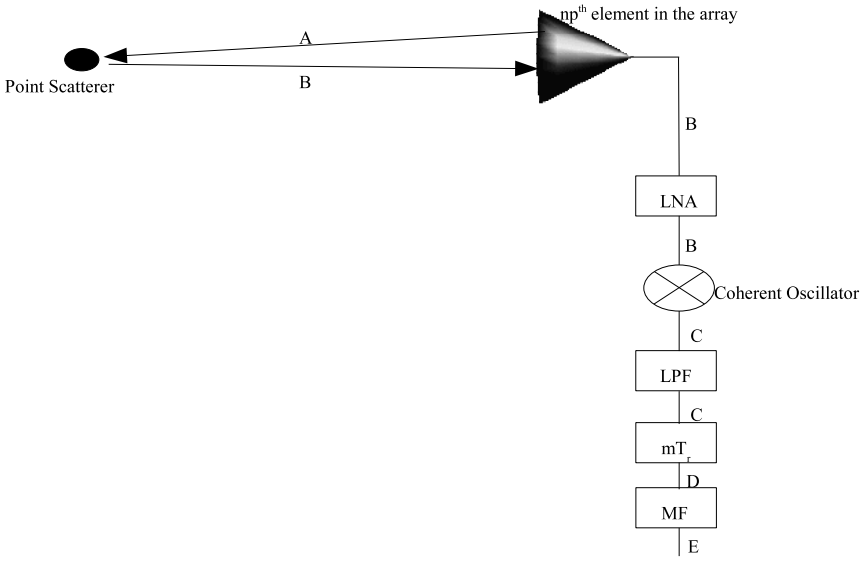

Figure 2.2: This figure represents the overall setup of the radar model.

Decomposing $u(t)$ provides more information about the pulse train. This decomposition is given by

$$u_M(t) = \sum_{m=0}^{M-1} u(t - mT_r), \tag{2.4}$$

where the summation of individual pulses $u(t)$ comprise the complete envelope $u_M(t)$ and T_r is the Pulse Repetition Interval.

An examination of the energy in the transmit signal provides an important check later in the development. Knowing the amount of energy in the transmit signal creates a ceiling for the received signal. If the energy in the received signal is greater than the transmitted signal, then there is an error within the mathematical calculations or there is an outside source providing energy to the system to spoof the radar. However, for this model, no spoofing is added to the system. Therefore, checking the energy in the returned signal is a good error check for the mathematics.

The energy in the transmit signal, normalized over one Pulse Repetition Interval (PRI), is defined as

$$E_M = \int_0^{mT_r} |s(t)|^2 dt, \tag{2.5}$$

where the subscript M indicates the number of pulses comprising the total energy and $s(t)$ is the transmitted signal. Allowing E_M to be defined only over a single pulse ($M = 1$), the fundamental energy becomes

$$\int_0^{T_r} |u(t)|^2 dt = \int_0^{T} (1)^2 dt = T \tag{2.6}$$

where T is the pulse width. Equation (2.6) is then normalized to achieve an energy value of one shown by

$$\frac{1}{T} \int_0^{T_r} |u(t)|^2 dt = 1. \tag{2.7}$$

Now adding the amplitude a_t, the energy in a single pulse becomes

$$E = \frac{1}{T} \int_0^{T_r} |a_t u(t)|^2 dt. \tag{2.8}$$

Since a_t is not a function of t, a_t^2 is pulled out of the integral. This action simplifies the energy equation for a single pulse to

$$E = \frac{a_t^2}{T} \int_0^{T_r} |u(t)|^2 dt = a_t^2. \tag{2.9}$$

Equation (2.7) states that this integral equals one. Therefore, the energy in a single pulse with amplitude a_t must equal a_t^2. Then, due to integration, the total energy in the transmitted signal is scaled by a factor of M, the number of pulses. Modifying (2.5), the total energy in M pulses is

$$E_M = \int_0^{MT_r} |s(t)|^2 dt = M a_t^2. \tag{2.10}$$

The transmit signal is now defined and some energy constraints are placed on the signal for error detection later in the development. A point scatter reflects the transmit signal back in the direction of the radar. This returned signal carries

information about the point scatterer. To gather this information, the received signal needs examination.

2.3 Received Signal

The received signal, labeled 'B' in Fig. 2.2, is the same as the transmitted signal with two differences. The first difference is an added Doppler shift f_d due to the relative velocity between the aircraft and the target. The second difference is a time delay to the np^{th} element, τ_{np}. Incorporating these differences, the received signal $r(t)$ becomes

$$r_{np}(t) = s(t - \tau_{np})e^{j2\pi f_d(t-\tau_{np})}. \tag{2.11}$$

An assumption is made here that all of the antenna elements are in the far field and therefore the Doppler shift variation across the elements is negligible. Assuming negligible Doppler shift simplifies the math later in the development. The time delay is needed due to the returned signal striking the array in a non-parallel fashion. Tracking time delays is necessary to be able to coherently add the phases and steer the array.

Before proceeding to the development of the received signal, there is a condition that must be considered. This condition is Doppler foldover or Doppler ambiguity. Doppler foldover occurs when the Doppler shift is greater than the Pulse Repetition Frequency (PRF) f_r. Therefore, as a check for ambiguity, the Doppler frequency is normalized by the PRF,

$$\bar{\omega} = \frac{f_d}{f_r} \tag{2.12}$$

where $\bar{\omega}$ represents the normalized Doppler frequency. If $\bar{\omega} > \left|\frac{1}{2}\right|$, then there is Doppler ambiguity. Otherwise, the Doppler frequency is unambiguous.

Looking back at the received signal in (2.11), there is a time delay component that requires understanding. To find the total signal delay to each element, a summation of the total round trip time of the signal (T_R) and the delay from the

reference element to the np^{th} element ($\tau_{np}^{'}$) is performed,

$$\tau_{np} = T_R + \tau_{np}^{'}. \tag{2.13}$$

The reference time delay requires further attention. $\tau_{np}^{'}$ describes the relationship between the np^{th} element to that of the reference element. This distance is otherwise known as the differential delay [1]. This delay is a projection of the unit vector in the direction of the target (described in terms of θ and ϕ) onto the vector describing the location of the element from the reference element (d_{np}) divided by the speed of light c. This projection results in

$$\tau_{np}^{'} = \frac{\hat{k}(\theta, \phi) \cdot d_{np}}{c}. \tag{2.14}$$

Expanding $\hat{k}$ and d_{np}, $\tau_{np}^{'}$ becomes

$$\tau_{np}^{'} = \frac{[\cos\theta \sin\phi \hat{x} + \cos\theta \cos\phi \hat{y} + \sin\theta \hat{z}] \cdot [-nd_x \hat{x} - pd_z \hat{z}]}{c}. \tag{2.15}$$

The array exists only in the x and z-axis, therefore the $\hat{y}$ term goes to zero resulting in

$$\tau_{np}^{'} = \frac{-nd_x \cos\theta \sin\phi - pd_z \sin\phi}{c}. \tag{2.16}$$

Now that the time delay is known, a conversion of the time delay into the spatial domain is necessary due to a phase delay acting on the original and Doppler shift frequencies. To convert (2.16) into the spatial domain, both sides of the equation are multiplied by ω_o

$$\omega_o \tau_{np}^{'} = \omega_o \frac{-nd_x \cos\theta \sin\phi - pd_z \sin\phi}{c}. \tag{2.17}$$

To help simplify (2.17), the variables ϑ_x and ϑ_z and are assigned

$$\vartheta_x = \frac{d_x \cos\theta \sin\phi}{\lambda_o} \tag{2.18}$$

and

$$\vartheta_z = \frac{d_z \sin\theta}{\lambda_o}. \tag{2.19}$$

By assigning the variables, (2.17) becomes

$$\omega_o \tau_{np}^{'} = -2\pi(n\vartheta_x + p\vartheta_z). \tag{2.20}$$

With a better understanding of $\tau_{np}^{'}$ and issues regarding Doppler foldover, development of the received signal in (2.11) continues. The transmitted signal in (2.3) is inserted into (2.11) producing

$$r_{np}(t) = a_r u_M(t - \tau_{np}) e^{j2\pi f_o(t-\tau_{np})} e^{j2\pi f_d(t-\tau_{np})} e^{j\psi}, \tag{2.21}$$

where ψ is the random starting phase, a_r is the received signal amplitude, and f_o is the transmit frequency. The parameter a_r will be much smaller than a_t. This reduction in signal strength is due to radar range equation effects. Substituting the total time delay in gives

$$r_{np}(t) = a_r u_M(t - T_R - \tau_{np}^{'}) e^{j2\pi(f_o+f_d)(t-T_R-\tau_{np}^{'})} e^{j\psi}. \tag{2.22}$$

At this point another assumption is made. This radar model is only for narrowband operations. This assumption means the time delay $\tau_{np}^{'}$ to each element is much smaller than the pulse width. Therefore, the time delay within the unit pulse of the signal can be ignored. If the transmitted pulse was a wideband pulse, there would be decorrelation across the face of the array which would need to be accounted for.

This assumption reduces (2.22) to,

$$r_{np}(t) = a_r u_M(t - T_R) e^{j2\pi(f_o+f_d)(t-T_R-\tau_{np}^{'})} e^{j\psi}. \tag{2.23}$$

Expanding the exponential terms produces

$$r_{np}(t) = a_r u_M(t - T_R) e^{j2\pi(f_o+f_d)t} e^{-j2\pi(f_o+f_d)T_R} \underbrace{e^{-j2\pi(f_o+f_d)\tau_{np}^{'}}} e^{j\psi}. \tag{2.24}$$

Examining the bracketed term, there is a $2\pi f_o \tau_{np}^{'}$ term which is also written as $\omega_o \tau_{np}^{'}$. Substituting (2.20) in, the bracketed exponential term is written as

$$e^{j2\pi f_d \tau_{np}^{'}} e^{j2\pi(n\vartheta_x + p\vartheta_z)}. \tag{2.25}$$

Rewriting (2.24) with this expanded exponential, the received signal becomes

$$r_{np}(t) = a_r u_M(t - T_R) e^{j2\pi(f_o+f_d)t} \underbrace{e^{-j2\pi(f_o+f_d)T_R} e^{-2\pi f_d \tau_{np}^{'}}} e^{j2\pi(n\vartheta_x+p\vartheta_z)} e^{j\psi}. \tag{2.26}$$

At this point, all the bracketed exponential terms in (2.26) are not a function of time. Therefore, these terms maintain a constant value over the duration of the pulse and are rolled into the ψ term. No information is lost in doing combing these terms. Later in the development, the $e^{j\psi}$ term and all the other exponentials that it encompasses, is taken into account. The received signal now equals

$$r_{np}(t) = a_r u_M(t - T_R) e^{j2\pi(f_o+f_d)t} e^{j2\pi(n\vartheta_x+p\vartheta_z)} e^{j\psi}. \tag{2.27}$$

At this point in the model, the signal in (2.27) has been received at the element and is ready for signal processing. There are steps that happen at this point in real world operations that are not simulated. First, the received signal is passed through a low noise power amplifier. Then the signal is sent through a coherent oscillator, labeled 'C' in Fig. 2.2. The oscillator strips the carrier frequency from the received

signal leaving the signal at baseband. After these two steps, the received signal now looks like,

$$r_{np}(t) = a_r u_M(t - T_R) e^{j2\pi f_d t} e^{j2\pi(n\vartheta_x + p\vartheta_z)} e^{j\psi}. \tag{2.28}$$

The next step in the signal processing involves adding (2.12) to (2.28). This process expands the equation giving

$$r_{np}(t) = \sum_{m=0}^{M-1} a_r u(t - T_R - mT_r) e^{j2\pi f_d t} e^{j2\pi(n\vartheta_x + p\vartheta_z)} e^{j\psi}. \tag{2.29}$$

At this point, the signal is at 'D' in Fig. 2.2. The received signal is now ready to be Matched Filtered (MF). This process introduces the Time Frequency Auto Correlation Function (TFACF). The MF process is the convolution of the transmitted signal and the received signal,

$$\chi_{np}(t) = \int_{-\infty}^{\infty} r_{np}(t) h(\tau - t) dt. \tag{2.30}$$

where χ represents the MF output and $h(t)$ is the matched filter impulse response. Since this model match filters pulse-by-pulse, the impulse response is simply the complex conjugate of the time reversed transmitted signal, $h(t) = u^*(-t)$. Substituting the received signal and $u^*(-t)$ into (2.30) results in

$$\chi_{np}(t) = \int_{-\infty}^{\infty} \sum_{m=0}^{M-1} a_r u(t - T_R - mT_r) e^{j2\pi f_d t} e^{j2\pi(n\vartheta_x + p\vartheta_z)} e^{j\psi} u^*(t - \tau) dt. \tag{2.31}$$

Pulling the terms not dependant on τ out of the integral gives

$$\chi(t) = a_r e^{j2\pi(n\vartheta_x + p\vartheta_z)} e^{j\psi} \int_{-\infty}^{\infty} \sum_{m=0}^{M-1} u(t - T_R - mT_r) u^*(t - \tau) e^{j2\pi f_d t} dt. \tag{2.32}$$

Adjusting the notation of the equation, the summation is removed from the equation and noted in the subscript.

$$\chi_{mnp}(t) = a_r e^{j2\pi(n\vartheta_x + p\vartheta_z)} e^{j\psi} \underbrace{\int_{-\infty}^{\infty} u(\tau - T_R - mT_r) u^*(\tau - t) e^{j2\pi f_d \tau} d\tau}. \tag{2.33}$$

This underlined section is the TFACF labeled Φ.

The next couple of steps focus on the TFACF. First to simplify the TFACF, a change of variables is performed with the integral. This change of variables is completed by first letting $\beta = t - T_R - mT_r$ which results in $t = \beta + T_R + mT_r$ and $\frac{d\beta}{d\tau} = 1$, modifying the TFACF expression to

$$\Phi(\tau, f_d) = \int_{-\infty}^{\infty} u(\beta) u^*(\beta + T_R + mT_r - \tau) e^{j2\pi f_d(\beta + \underbrace{T_R + mT_r}_{})} d\beta. \tag{2.34}$$

The bracketed section of the exponential has no dependance on β. Therefore, these exponentials are pulled out front of the integral and incorporated into the rest of the MF expression. This leaves the expression, coming of the MF at 'E' in Fig. 2.2, for the TFACF as

$$\Phi(\tau, f_d) = \int_{-\infty}^{\infty} u(\beta) u^*(\beta + T_R + mT_r - \tau) e^{j2\pi f_d \beta} d\beta. \tag{2.35}$$

Reviewing the MF expression (2.33) after simplifying the TFACF, the overall expression becomes

$$\chi_{mnp}(t) = a_r e^{j2\pi(n\vartheta_x + p\vartheta_z)} e^{j\psi} e^{j2\pi f_d T_R} \underbrace{e^{j2\pi f_d m T_r}}_{} \int_{-\infty}^{\infty} u(\beta) u^*(\beta + T_R + mT_r - \tau) e^{j2\pi f_d \beta} d\beta, \tag{2.36}$$

where the underlined exponential has the $f_d T_r$ term. As defined earlier, $f_d T_r$ equals the normalized Doppler frequency $\bar{\omega}$. Therefore, rewriting this equation with the $\bar{\omega}$

notation and moving some terms around results in

$$\chi_{mnp}(t) = \underbrace{a_r e^{j\psi} e^{j2\pi f_d T_R}} e^{j2\pi(n\vartheta_x + p\vartheta_z)} e^{j2\pi m\bar{\omega}} \int_{-\infty}^{\infty} u(\beta)u^*(\beta + T_R + mT_r - \tau)e^{j2\pi f_d \beta} d\beta. \quad (2.37)$$

Examining the bracketed portion, these terms are all constant terms that have no dependance on time or pulse number. Therefore, all of these variables are rolled into one variable α_t which provides a single complex amplitude term corresponding to a point scatter. This simplification leaves the MF expression as

$$\chi_{mnp}(t) = \alpha_t e^{j2\pi(n\vartheta_x + p\vartheta_z)} e^{j2\pi m\bar{\omega}} \int_{-\infty}^{\infty} u(\beta)u^*(\beta + T_R + mT_r - \tau)e^{j2\pi f_d \beta} d\beta. \quad (2.38)$$

! The radar model will be continued to be built from this point further implementing key assumptions. However, this point will be revisited later in Chapter three as the starting point for exploring the effects of the TFACF on the radar model.

At this point, two assumptions are made within the TFACF. These assumptions are that the received signal is matched perfect in range and in Doppler. The first assumption is that the target range cell corresponds to a range delay $\tau = T_R + mT_r$. Breaking this assumption down, there are really two parts to this assumption. The first part is that there is a target present at this point in time and space. This assumption will still be held through out this research. The second part to this assumption is that when matching this location, the range cell matches perfectly. For the research, this assumption is removed allowing for the range cell to vary $\frac{1}{2}$ a chip width. Implementing the assumption that the pulses are matched perfectly in range into (2.38), the expression becomes

$$\boldsymbol{\chi}_{mnp}(t) = \alpha_t e^{j2\pi(n\vartheta_x + p\vartheta_z)} e^{j2\pi m\bar{\omega}} \int_{-\infty}^{\infty} u(\beta)u^*(\beta)e^{j2\pi f_d \beta} d\beta. \quad (2.39)$$

The second assumption is that the transmitted waveform is Doppler tolerant. In effect, this assumption removes the Doppler shift exponent from the TFACF integral, reducing the integral to

$$\int_{-\infty}^{\infty} u(\beta)u^*(\beta)d\beta = 1. \tag{2.40}$$

With the energy being defined in (2.7) equaling one, this integral also evaluates to one. With the TFACF equaling one, there is no effect on the MF in the radar model.

These assumptions make the generic mnp^{th} received matched filtered signal expression for a specific range cell k (target location) to be

$$\chi_{mnpk} = \alpha_t e^{j2\pi(n\vartheta_x + p\vartheta_z)} e^{j2\pi m\bar{\omega}}. \tag{2.41}$$

Equation (2.41) is the final expression for the matched filter output which contains the terms ϑ_x, ϑ_z, and $\bar{\omega}$. These terms contain information in space and time about the returned pulse. An examination of the role that these terms play is now necessary.

2.4 Steering Vector

Equation (2.41) describes the received signal in space and time at a particular range cell. A rearrangement of this equation into a linear algebra framework simplifies simulations. For insight into how the linear algebra will help, (2.41) is rewritten as

$$\boldsymbol{\chi}_k = \alpha_t e^{j2\pi[(0:N-1)^H\vartheta_x + (0:P-1)^H\vartheta_z]} e^{j2\pi(0:M-1)^H\bar{\omega}} \tag{2.42}$$

where H represents the Hermitian operation. Equation (2.42) results in a $NMP \times 1$ vector containing all mnp returns for range cell k.

Each vector within (2.42) is a different steering vector. These three steering vectors describe the phase progression across azimuth channel elements,$\mathbf{a}(\vartheta_x)$,

$$\mathbf{a}(\vartheta_x) = \begin{bmatrix} e^{j2\pi\vartheta_x} & e^{j2\pi(2)\vartheta_x} & \dots & e^{j2\pi(N-1)\vartheta_x} \end{bmatrix}, \tag{2.43}$$

elevation channel elements, $\mathbf{e}(\vartheta_z)$,

$$\mathbf{e}(\vartheta_z) = \begin{bmatrix} e^{j2\pi\vartheta_z} & e^{j2\pi(2)\vartheta_z} & \dots & e^{j2\pi(N-1)\vartheta_z} \end{bmatrix}, \tag{2.44}$$

and across pulses, $\mathbf{b}(\bar{\omega})$,

$$\mathbf{b}(\bar{\omega}) = \begin{bmatrix} e^{j2\pi\bar{\omega}} & e^{j2\pi(2)\bar{\omega}} & \dots & e^{j2\pi(N-1)\bar{\omega}} \end{bmatrix}. \tag{2.45}$$

Combining the steering vectors is done using the Kronecker product to form the vector in (2.42). This new vector describing the phase progression from element-to-element and pulse-to-pulse is the steering vector, $\mathbf{v}$,

$$\mathbf{v} = \mathbf{e}(\vartheta_z) \otimes \mathbf{b}(\bar{\omega}) \otimes \mathbf{a}(\vartheta_x). \tag{2.46}$$

Placing the steering vector into (2.42), the new space-time snapshot describing each element and pulse return at range cell k is

$$\boldsymbol{\chi}_k = \alpha_t \mathbf{e}(\vartheta_z) \otimes \mathbf{b}(\bar{\omega}) \otimes \mathbf{a}(\vartheta_x). \tag{2.47}$$

2.5 Element Pattern

To create the element pattern, an assumption is made that all the elements are identical. Identical elements means each element has the same voltage pattern $f(\theta, \phi)$ and power pattern $g(\theta, \phi)$, where the power pattern is equal to the voltage pattern squared.

To create the element pattern, a simple cosine pattern in azimuth and elevation is used. This pattern creates a complete spherical shape surrounding the platform. Since the target of interest is located in front of the radar, there is no need to transmit or model the pattern behind the radar. Yet, no antenna is perfect and some energy is still effectively transmitted behind the radar. Therefore, a backlobe attenuation factor b_e is incorporated in the element pattern to represent energy transmitted behind the radar. This attenuation factor is typically modelled 30-dB lower than that of the mainlobe representing the concept that the energy from the antenna is transmitted forward at the target and not behind the radar where there is no target.

The element pattern and the array pattern are needed to be able to beamform the antenna. Since the element pattern was just found, the next step is to find the array pattern.

2.6 Array Pattern

The array pattern uses the element pattern generated to form the antenna pattern by coherently adding the signal transmitted from each element. This coherent addition creates the antenna beam. To steer this beam, relative time delays between elements create phase delays. These time delays were already found and are expressed in the steering vectors $\mathbf{a}(\vartheta_x)$ and $\mathbf{e}(\vartheta_z)$ These phase delays steer the beam in the elevation and azimuth. Upon receive, the returns are correctly scaled depending on how the antenna beam illuminates them. Therefore, the phase weights from the transmit are applied to the received returns.

When creating the array pattern, only two of the steering vectors are needed ($\mathbf{e}(\vartheta_z)$ and $\mathbf{a}(\vartheta_x)$). This need for only using the vectors $\mathbf{e}(\vartheta_z)$ and $\mathbf{a}(\vartheta_x)$ is due to the fact that the pattern only exists within the spatial domains. Since the steering vectors describe the phase progression across each element in the array, creating a

weighted array factor, $W(\theta, \phi)$, for all elements in the array is simply completed by

$$W(\theta, \phi) = [\mathbf{e}(\vartheta_x) \otimes \mathbf{a}(\vartheta_z)]^T \mathbf{1}. \tag{2.48}$$

Rewriting (2.48) in a different form,

$$W(\theta, \phi) = \sum_{p=0}^{P-1} \sum_{n=0}^{N-1} e^{j2\pi p \vartheta_z} e^{j2\pi n \vartheta_z}. \tag{2.49}$$

In an effort to simplify (2.49), the partial sum of a geometric series ($\sum_{q=0}^{r} a^q = \frac{1-a^{r+1}}{1-a}$) is applied. Applying the geometric series is allowed since there is a finite number of array elements. This application results in

$$W(\theta, \phi) = \frac{1 - e^{j2\pi P \vartheta_z}}{1 - e^{j2\pi \vartheta_z}} \frac{1 - e^{j2\pi N \vartheta_x}}{1 - e^{j2\pi \vartheta_x}}. \tag{2.50}$$

Examining (2.50), simple factoring from the exponentials results in

$$W(\theta, \phi) = \frac{e^{j\pi P \vartheta_z}}{e^{j\pi \vartheta_z}} \left(\frac{e^{-j\pi P \vartheta_z} - e^{j\pi P \vartheta_z}}{e^{-j\pi \vartheta_z} - e^{j\pi \vartheta_z}} \right) \frac{e^{j\pi N \vartheta_x}}{e^{j\pi \vartheta_x}} \left(\frac{e^{-j\pi N \vartheta_x} - e^{j\pi N \vartheta_x}}{e^{-j\pi \vartheta_x} - e^{j\pi \vartheta_x}} \right). \tag{2.51}$$

At this point, the exponentials contained within the parenthesis are recognized as sinusoids. Rewriting (2.51) with the sinusoids gives

$$W(\theta, \phi) = e^{j\pi(P-1)\vartheta_z} e^{j\pi(N-1)\vartheta_x} \left(\frac{\sin(\pi P \vartheta_z) \sin(\pi N \vartheta_x)}{\sin(\pi \vartheta_z) \sin(\pi \vartheta_x)} \right). \tag{2.52}$$

Substituting in the values of ϑ_x and ϑ_z reveals the angles that occur within the array pattern,

$$W(\theta, \phi) = e^{j \frac{\pi d_z}{\lambda_o} (P-1) \sin(\theta)} e^{j \frac{\pi d_x}{\lambda_o} (N-1) \cos(\theta) \sin(\phi)} \left(\frac{\sin(\frac{\pi d_z}{\lambda_o} P \sin\theta) \sin(\frac{\pi d_x}{\lambda_o} N \cos\theta \sin\phi)}{\sin(\frac{\pi d_z}{\lambda_o} \sin\theta) \sin(\frac{\pi d_x}{\lambda_o} \cos\theta \sin\phi)} \right) \tag{2.53}$$

Equation (2.53) is the final equation for the array factor. However, there are three special cases that must be addressed before continuing. The 'sin' term raises concern. When either ϕ or θ is at a value of zero, the term sin equals zero. This results in a $\frac{0}{0}$ case.

The first case dealt with is when $\phi = 0$. When ϕ equals zero, the azimuth portion of the array equation goes to zero. Using L'Hôpital's rule, the derivative of the numerator and the denominator is taken and the expression is then evaluated at $\phi = 0$,

$$W(\theta,0) = \frac{\left(e^{j\frac{\pi d_z}{\lambda_o}(P-1)\sin\theta}\right)(1)\left(\sin(\frac{\pi d_z}{\lambda_o}P\sin\theta)\right)}{\sin\left(\frac{\pi d_z}{\lambda_o}\sin\theta\right)} \frac{\left[\frac{d}{d\phi}\big|_0 = \cos\left(\frac{\pi d_x}{\lambda_o}N\cos\theta\cos\phi\right)\frac{\pi d_x}{\lambda_o}N\cos\theta\cos\phi\right]}{\frac{d}{d_\phi}\big|_0\sin\left(\frac{\pi d_x}{\lambda_o}\cos\theta\cos\phi\right)}. \quad (2.54)$$

Evaluating the above expression, the final response for the antenna pattern at $\phi = 0$ is

$$W(\theta,0) = Ne^{j\frac{\pi d_z}{\lambda_o}(P-1)\sin\theta}\left(\frac{\sin\left(\frac{\pi d_z}{\lambda_o}\right)P\sin\theta}{\sin\left(\frac{\pi d_z}{\lambda_o}\right)\sin\theta}\right). \quad (2.55)$$

The second case dealt with is when $\theta = 0$. Again, using L'Hôpital's rule the response for the antenna pattern is similar to that in (2.55),

$$W(0,\phi) = Pe^{j\frac{\pi d_x}{\lambda_o}(N-1)\sin\theta}\left(\frac{\sin\left(\frac{\pi d_x}{\lambda_o}\right)N\sin\theta}{\sin\left(\frac{\pi d_x}{\lambda_o}\right)\sin\theta}\right). \quad (2.56)$$

The third and last special case that needs to be addressed is when both ϕ and θ are equal to zero. Using the same method outlined above, the weighting factor becomes

$$W(0,0) = NP. \quad (2.57)$$

The array factor is now modeled accurately. However, it is symmetrical in the complete sphere. The array factor is multiplied by the element pattern to account for the back lobe attenuation. The product of this union provides for an accurate transmit antenna beam produced by the radar.

The antenna is now modeled accurately. This accurate model is necessary to implement later with the clutter model allowing for proper scaling of clutter returns. However, the next logical step is to examine the effects that thermal noise produces within the receiver elements.

2.7 Thermal Noise

Thermal noise or Additive White Gaussian Noise, is present at every array element. This noise is produced naturally within the elements themselves and must be accounted for within the model. Calculating thermal noise depends on the radar bandwidth and the standard (operating) temperature. Noise power, typically represented as σ^2, is equal to the product of the system bandwidth and the noise power spectral density N_o. N_o is a calculated from Boltzman's constant k and the standard temperature T_o.

Since thermal noise is unique to each separate element, the statistics of the noise in the spatial domain are mutually uncorrelated. The temporal domain is also mutually uncorrelated since it is white noise. This uncorrelation results in a space-time snapshot $\boldsymbol{\chi}_n$ describing thermal noise. Finding the covariance matrix for the thermal noise is completed using $\boldsymbol{\chi}_n$ and taking the expected value of the its outer product. However, this matrix is simplified due to the correlation along the diagonal of the matrix. Everywhere else in the matrix, the values are zero. Therefore, the thermal noise covariance matrix, $\mathbf{R}_n$, simplifies to

$$\mathbf{R}_n = \sigma^2 \mathbf{I}_{MNP}, \tag{2.58}$$

where $\mathbf{I}_{MNP}$ is an Identity matrix.

At this point, the model is almost complete. One factor not incorporated into the model still needs examining. When the radar transmits a signal, signals are returned from more than just the point scatterer target. Returns from the ground, sea and atmosphere are also received by the radar. These returns are called clutter.

2.8 Clutter

The clutter model used is for this model is one that is generally accepted within the radar community. Sources of clutter are limited to those produced by the Earth's surface (land and sea). The effects of clutter from the sea and ground are rather large when compared to the clutter from the atmosphere. The Earth is assumed perfectly spherical with a $\frac{4}{3}$ effective radius of the Earth.

A limitation of the radar model is only inspecting a single range cell at a given moment. The range cell exists in a complete circle encompassing the aircraft. This ring is called the clutter ring. Each ring is divided into N_c patches. The clutter model is a summation of all N_c patches creating the clutter ring for a specific range cell. Typically, the range cell of interest is the target location.

Defining each clutter patch is the beginning. Each patch has a distinguished reflectivity that is dependant on the elevation and azimuth angles. To begin with, the elevation angle is calculated θ_c. Referencing Fig. 2.3, θ_c is found using the law of cosines

$$\theta_c = -\sin^{-1}\frac{R_c^2 + h_a(h_a + 2a_e)}{2R_c(a_e + h_a)}, \tag{2.59}$$

where R_c is the range to the clutter patch, h_a is the height of the aircraft, and a_e is the effective radius of the earth.

The next step is to find the grazing angle. The grazing angle is defined by the tangential line from the clutter patch to the line from the patch to the aircraft, as

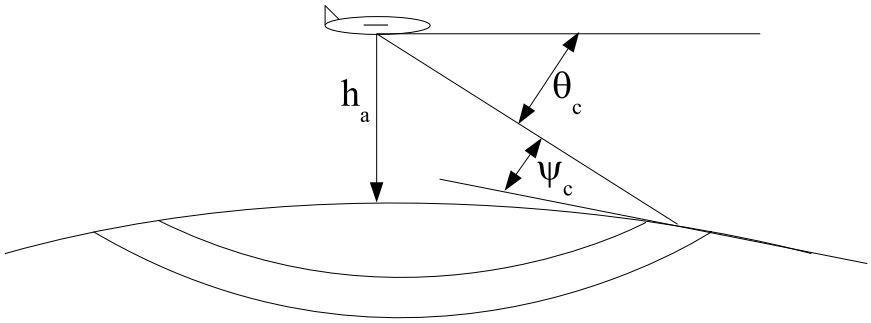

Figure 2.3: This represents the clutter geometry. The view is from the side providing insight into the calculation of the grazing and clutter angles.

seen in Fig. 2.3, resulting in a expression for the grazing angle as

$$\psi_c = -\sin^{-1}\frac{R_c^2 - h_a(h_a + 2a_e)}{2R_c a_e}. \tag{2.60}$$

Every radar contends with return ambiguities. This model incorporates any possible clutter ring ambiguities that occur if the horizon range extends greater than the unambiguous range of the radar where the unambiguous range is defined as $R_u = \frac{cT_r}{2}$ [5]. The horizon range is found at the point where the grazing angle equals zero,

$$R_h = \sqrt{h_a^2 + 2H_a a_e}. \tag{2.61}$$

The number of range ambiguities is then found by

$$N_r = \frac{R_h}{R_u}. \tag{2.62}$$

If $R_h \geq R_c N_r$, N_r is rounded up, otherwise N_r is rounded down.

At this point, a 3-D space-time snapshot of the clutter for a specific range cell k is expressed as

$$\boldsymbol{\chi}_c = \sum_{i=0}^{N_r-1}\sum_{l=0}^{N_c-1} \alpha_{il}\mathbf{e}_{il}(\vartheta_z) \otimes \mathbf{b}_{il}(\bar{\omega}) \otimes \mathbf{a}_{il}(\vartheta_x). \tag{2.63}$$

This expression characterizes returns for every clutter patch around all N_r rings for a specific range cell k. However, the random clutter patch amplitude α_{il} is unknown.

Finding α_{il} starts with determining the effective RCS of the clutter patch, σ_{il}. The RCS patch is found by multiplying the area of the patch by the ground reflectivity, $\sigma_o(\theta_i, \phi_l)$, for the patch,

$$\sigma_{il} = \sigma_o(\theta_i, \phi_l) R_i \Delta\phi \Delta R \sec\psi_i. \tag{2.64}$$

The ground reflectivity is found using a constant gamma model for clutter [5] and is defined as

$$\sigma_o(\theta_,\phi_l) = \gamma \sin\psi_i. \tag{2.65}$$

The area of the patch depends on the range R_i as well as the grazing angle ψ_i to the patch. $\Delta\phi$, defined as $\frac{2\pi}{N_c}$, is the angular extent of the patch while ΔR is the range resolution, defined as $\frac{c}{2B}$.

With the clutter patch RCS, an element Clutter to Noise Ratio (CNR) is found using the radar range equation. Finding the CNR requires array and element patterns. This need for the patterns is why time was spent earlier developing those section of the model. The CNR for a single element is defined as

$$\boldsymbol{\xi}_{il} = \frac{P_t G_t(\theta_i, \phi_l) g(\theta_i, \phi_l) \lambda_o^2 \sigma_{il}}{(4\pi)^3 N_o B L_s R_i^4}, \tag{2.66}$$

where P_t is the power transmitted, L_s is the loss in the system, λ is the wavelength, $G_t(\theta_i, \phi_l)$ is the array pattern, and $g(\theta_i, \phi_l)$ is the element pattern.

Now the random amplitude can be defined as

$$\alpha_{il} = \sigma^2 \xi_{il}. \tag{2.67}$$

All this development enables a 3D space-time snapshot to be rewritten as

$$\boldsymbol{\chi}_c = \sigma^2 \sum_{i=0}^{N_r-1} \sum_{l=0}^{N_c-1} \sigma^2 \xi_{il} \mathbf{e}_{il}(\vartheta_z) \otimes \mathbf{b}_{il}(\bar{\omega}) \otimes \mathbf{a}_{il}(\vartheta_x). \tag{2.68}$$

In order to find the clutter covariance matrix, the expected value of the outer product of (2.68) is performed

$$\mathbf{R}_c = E\{\boldsymbol{\chi}_c \boldsymbol{\chi}_c^H\}, \tag{2.69}$$

which is rewritten as

$$\mathbf{R}_c = \sum_{i=0}^{N_r-1} \sum_{l=0}^{N_c-1} \sigma^2 \xi_{il} \mathbf{e}_{il}(\vartheta_z) \mathbf{e}_{il}^H(\vartheta_z) \otimes \mathbf{b}_{il}(\bar{\omega}) \mathbf{b}_{il}^H(\bar{\omega}) \otimes \mathbf{a}_{il}(\vartheta_x) \mathbf{a}_{il}^H(\vartheta_x). \tag{2.70}$$

The radar model is now completely built covering the radar from transmission of the signal to the processing of the received signal. An acknowledgement is made that outside interferers such as clutter returns and thermal noise in the receivers effect the detection of targets. Therefore, these interferes are modeled and incorporated with in the radar model. At this point, the research continues onto looking at the effects that the TFACF will have on the model.

III. Time Frequency Auto Correlation Function Developement

The Ambiguity Function (AF) is a tool to analyze ambiguities that occur within waveforms. The AF is simply the magnitude of the Time Frequency Auto Correlation Function (TFACF), the matched filter output of the signal, squared. This matched filter produces an autocorrelation of the signal. However, there is a Doppler shift that is incorporated in the returned signal. This shift results in a cross-correlation producing the overall TFACF.

3.1 Generic Waveform Model

Looking back at chapter two, an assumption was made to approximate the TFACF in (2.38) to one. At this point, the expression for the TFACF is needed for placement within the model.

The first step in building the generic TFACF is the the transmit signal given by

$$s(t) = \sum_{m=0}^{M-1} \sum_{q=0}^{Q-1} u(t - mT_r - qT_c) e^{j\psi_{mq}}, \tag{3.1}$$

where ψ_{mq} is the random starting phase of the signal, T_r is the PRI, T_c is the chip width within the pulse, and Q is the number of chips within each pulse. The received signal is modeled as the transmit signal with a time delay to the target as well as a Doppler shift on the signal. This received signal is written as

$$r(t) = s(t - T_R) e^{j2\pi f_d (t - T_R)} \tag{3.2}$$

where T_R is the round trip time to the point scatterer.

Since the TFACF is the section under examination, a closer look at it is desired. The TFACF is defined as

$$\Phi(\tau, f_d) = \int_{-\infty}^{\infty} r(t)h(\tau - t)dt \tag{3.3}$$

where $h(t)$ is the matched filter impulse response. Since each pulse is matched filtered upon receive, the matched filter impulse response is considered the conjugate of the transmitted signal, $h(t) = s^*(-t)$. Substituting into the TFACF for $r(t)$ and $h(t)$ results in

$$\Phi(\tau, f_d) = \int_{-\infty}^{\infty} s(t - T_R)e^{j2\pi f_d t}s^*(t - \tau)dt. \tag{3.4}$$

At this point, T_R and τ are providing the same delay action on the equation. So the TFACF equation simplifies to

$$\Phi(\tau - T_R, f_d) = \int_{-\infty}^{\infty} s(t)e^{j2\pi f_d t}s^*(t - \tau + T_R)dt. \tag{3.5}$$

Therefore, inserting the transmit signal into the TFACF results in

$$\Phi(\tau - T_R, f_d) = \int_{-\infty}^{\infty} \sum_{m=0}^{M-1}\sum_{q=0}^{Q-1} u(t - mT_r - qT_c)e^{j\psi_{mq}}e^{j2\pi f_d t} \sum_{a=0}^{M-1}\sum_{b=0}^{Q-1} u(t - aT_r - bT_c - \tau + T_R)e^{-j\psi_{ab}}dt, \tag{3.6}$$

where a and b represent the returned signal pulse and chip numbers, respectively. This is required to account for offsets between the transmit and received signals. At this point, an assumption is made that there are no multiple time around returns. Therefore, this assumption indicates that the pulses are matched ($n = a$), allowing

one of the summations to collapse leaving

$$\Phi(\tau - T_R, f_d) = \sum_{m=0}^{M-1} \int_{-\infty}^{\infty} \sum_{q=0}^{Q-1} u(t - mT_r - qT_c) e^{j\psi_{mq}} \sum_{b=0}^{Q-1} u(t - mT_r - bT_c - \tau + T_R) e^{-j\psi_{mb}} e^{j2\pi f_d t} dt. \quad (3.7)$$

Another assumption is made at this point regarding the TFACF. A limitation is placed on the shift of the signal as it is received. The pulse will not be more than a half chip width off, $\left|\tau \leq \frac{T_R - T_c}{2}\right|$. This assumption allows for the target SNR to remain constant. With this limitation, there are three different cases that must be considered. These cases are when $\tau - T_R < 0$, $\tau - T_R = 0$, and $\tau - T_R > 0$. At this point, a deeper examination of these three cases is completed.

3.2 Examination of the Time Frequency Auto Correlation Function

There are three cases that arise due to the limitation placed on the pulse being less than one half of a chip off, $\tau - T_R < 0$, $\tau - T_R = 0$, and $\tau - T_R > 0$.

3.2.1 Less than Case ($\tau - T_R < 0$). This case occurs when the received signal is early. Figure 3.1 illustrates how the transmitted pulses corresponds to the received pulse and thus how the chips within the pulse line up. Referencing Fig 3.1 assists in determining the limits of integration.

Since there are two different phases from the received signal that are being matched to the transmitted signal, two different integrals are required. The different phases occur due to the phase cancellation of the perfectly matched pulse and the lack of phase cancellation with the offset matched pulse. Referencing Fig 3.1, the limits of integration are determined.

The perfectly matched signal is $mT_r + qT_c$ for the lower limit and the upper limit is $mT_r + (q+1)T_c + \tau - T_R$. The limits for the signal that has offsetting phases

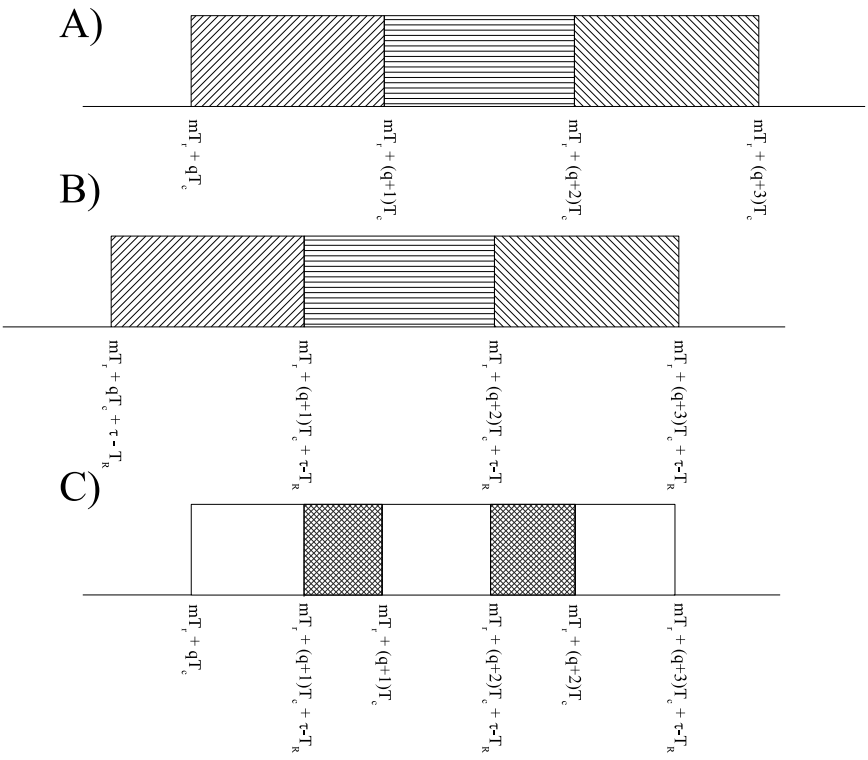

Figure 3.1: The case is when the received chip is matched early. The phase offset are shown by a cross-hatch while the equal phase cases are blank.

are $mT_r + (q+1)T_c + \tau - T_R$ for the lower limit and $mT_r + (q+1)T_c$ for the upper limit. Therefore, the TFACF si now written as

$$\Phi(\tau - T_R < 0, f_d) = \sum_{m=0}^{M-1}\sum_{q=0}^{Q-1}\int_{mT_r+qT_c}^{mT_r+(q+1)T_c+\tau-T_R} e^{j\psi_{mq}}e^{-j\psi_{mq}}e^{j2\pi f_d t}dt + \int_{mT_r+(q+1)T_c+\tau-T_R}^{mT_r+(q+1)T_c} e^{j\psi_{mq}}e^{-j\psi_{m,q+1}}e^{j2\pi f_d t}dt. \quad (3.8)$$

The phases in the first integral cancel each other out leaving

$$\sum_{m=0}^{M-1}\sum_{q=0}^{Q-1}\int_{mT_r+qT_c}^{mT_r+(q+1)T_c+\tau-T_R} e^{j2\pi f_d t}dt + \int_{mT_r+(q+1)T_c+\tau-T_R}^{mT_r+(q+1)T_c} e^{j\psi_{mq}}e^{-j\psi_{m,q+1}}e^{j2\pi f_d t}dt. \quad (3.9)$$

The solution to the first integral is

$$\frac{1}{j2\pi f_d}e^{j2\pi f_d t}\Big|_{mT_r+qT_c}^{mT_r+(q+1)T_c+\tau-T_R}. \quad (3.10)$$

Evaluating this solution by inserting the limits of integration in for t gives

$$\frac{1}{j2\pi f_d}\left[e^{j2\pi f_d(mT_r+(q+1)T_c+\tau-T_R)} - e^{j2\pi f_d(mT_r+qT_c)}\right]. \quad (3.11)$$

Pulling out the common terms within the expression leaves

$$\frac{1}{j2\pi f_d}e^{j2\pi f_d qT_c}e^{j2\pi f_d mT_r}\left[e^{j2\pi f_d(T_c+\tau-T_R)} - 1\right]. \quad (3.12)$$

The exponential term containing T_r is pulled outside of the summation over Q since it is dependant on M. This term occurs within the second integral as well. Since the T_r term is dependant only on M, it forms the steering vector $\mathbf{b}(\bar{\omega})$.

Looking back at (3.12), a exponential term is pulled out of the brackets giving

$$\frac{e^{j2\pi f_d q T_c}}{j2\pi f_d} e^{j\pi f_d(T_c+\tau-T_R)} \left[e^{j\pi f_d(T_c+\tau-T_R)} - e^{-j\pi f_d(T_c+\tau-T_R)}\right]. \tag{3.13}$$

At this point, recognition is made that this form is similar to Euler's identity. The numerator and denominator are multiplied by $(T_c + \tau - T_R)$ to complete Euler's identity allowing the equation to simplify to

$$(T_c + \tau - T_R) e^{j2\pi f_d q T_c} e^{j\pi f_d(T_c+\tau-T_R)} \text{sinc}[f_d(T_c + \tau - T_R)]. \tag{3.14}$$

Equation (3.14) is the final expression for the first integral. Now the second integral needs to be solved,

$$\int_{mT_r+(q+1)T_c+\tau-T_R}^{mT_r+(q+1)T_c} e^{j\psi_{mq}} e^{-j\psi_{m,q+1}} e^{j2\pi f_d t} dt. \tag{3.15}$$

The phase exponentials are combined together. Since they have no dependance on t, the phase exponentials are pulled outside the integral resulting in

$$e^{j(\psi_{mq}-\psi_{m,q+1})} \int_{mT_r+(q+1)T_c+\tau-T_R}^{mT_r+(q+1)T_c} e^{j2\pi f_d t} dt \tag{3.16}$$

The answer for the solved the integral is

$$e^{(\psi_{mq}-\psi_{m,q+1})} \frac{1}{j2\pi f_d} e^{j2\pi f_d t} \Big|_{mT_r+(q+1)T_c+\tau-T_R}^{mT_r+(q+1)T_c} \tag{3.17}$$

Evaluating the solution with the limits of integration, the expression becomes

$$e^{(\psi_{mq}-\psi_{m,q+1})} \frac{1}{j2\pi f_d} \left[e^{j2\pi f_d(mT_r+(q+1)T_c)} - e^{j2\pi f_d(mT_r+(q+1)T_c+\tau-T_R)}\right] \tag{3.18}$$

Pulling out the common terms from the expression gives

$$e^{j2\pi f_d m T_r} e^{(\psi_{mq}-\psi_{m,q+1})} \frac{1}{j2\pi f_d} e^{j2\pi f_d (q+1)T_c} \left[1 - e^{j2\pi f_d(\tau - T_R)}\right] \tag{3.19}$$

Again, the exponential term containing the mT_r is pulled out ahead of the summation over Q due to it being folded into the steering vector $\mathbf{b}(\bar{\omega})$. Euler's identity is found by pulling a term out from the brackets resulting in

$$-e^{(\psi_{mq}-\psi_{m,q+1})} \frac{e^{j2\pi f_d (q+1)T_c}}{j2\pi f_d} e^{j\pi f_d(\tau - T_R)} \left[e^{j\pi f_d(\tau - T_R)} - e^{-j\pi f_d(\tau - T_R)}\right]. \tag{3.20}$$

Completing the equation to form a proper Euler's identity, the numerator and denominator are multiplied by $\tau - T_R$,

$$- e^{(\psi_{mq}-\psi_{m,q+1})}(\tau - T_R) e^{j2\pi f_d (q+1)T_c} e^{j\pi f_d(\tau - T_R)} \text{sinc}[f_d(\tau - T_R)], \tag{3.21}$$

which is the final form for the second integral.

Combining (3.14) and (3.21), the overall expression for $-\frac{T_c}{2} < \tau - T_R < 0$ is

$$\begin{aligned}\Phi(\tau - T_R < 0, f_d) = \sum_{m=0}^{M-1} e^{j2\pi f_d m T_r} \sum_{q=0}^{Q-1} (T_c + \tau - T_R) e^{j2\pi f_d q T_c} e^{j\pi f_d (T_c + \tau - T_R)} \\ \text{sinc}[f_d(T_c + \tau - T_R)] - e^{(\psi_{mq}-\psi_{m,q+1})}(\tau - T_R) \\ e^{j2\pi f_d (q+1)T_c} e^{j\pi f_d(\tau - T_R)} \text{sinc}[f_d(\tau - T_R)].\end{aligned} \tag{3.22}$$

3.2.2 Greater than Case ($\tau - T_R > 0$). This case occurs when the received signal appears to be late. Figure 3.2 illustrates how the received pulse matches up to the transmitted pulse as well as how the chips within the pulses are offset. Referencing Fig 3.2 provides insight into the limits of integration.

Just as in the less than case, this case also has two integrations due to the phase shifts. The first integral with matching phases, the lower limit is $mT_r + qT_c + \tau - T_R$

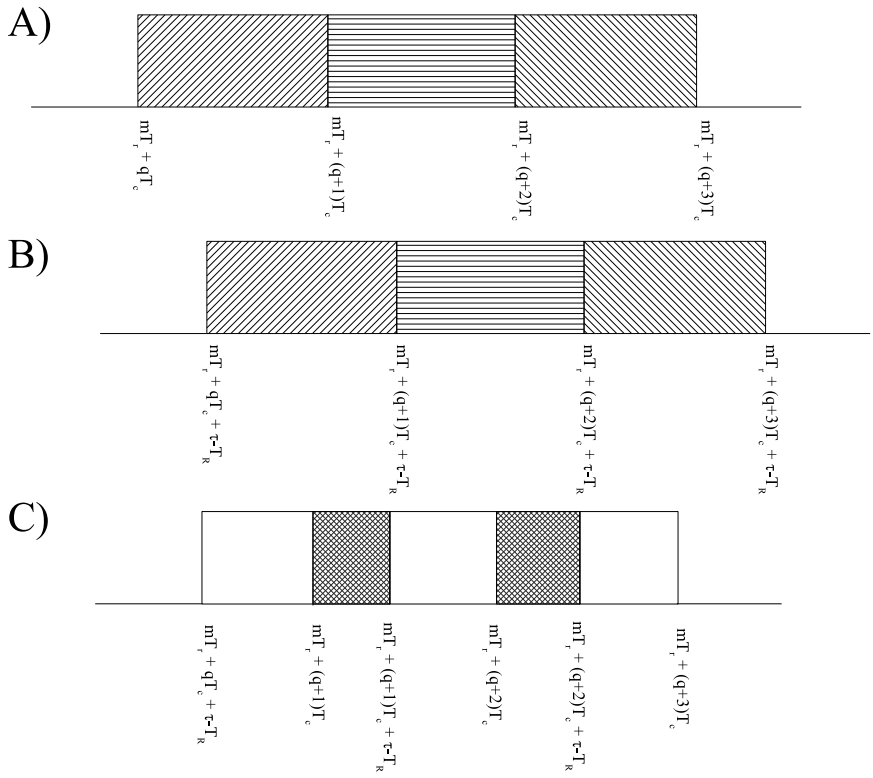

Figure 3.2: This case occurs when the received chip arrives late. The equal phases, which cancel each other out, are represented by blank space while the offset phases that interferer with each other are cross-hatched.

while the upper limit is $mT_r + (q+1)T_c$. The offset phase integral has upper and lower limits of $mT_r + qT_c + \tau - T_R$ and $mT_r + qT_c$, respectively, resulting in

$$\Phi(\tau - T_R > 0, f_d) = \sum_{m=0}^{M-1}\sum_{q=0}^{Q-1}\int_{mT_r+qT_c+\tau-T_R}^{mT_r+(q+1)T_c} e^{j\psi_{mq}}e^{-j\psi_{mq}}e^{j2\pi f_d t}dt + \int_{mT_r+(q+1)T_c}^{mT_r+(q+1)T_c+\tau-T_R} e^{j\psi_{mq}}e^{-j\psi_{m,q+1}}e^{j2\pi f_d t}dt. \quad (3.23)$$

By canceling out the common phase terms, the equation becomes

$$\sum_{m=0}^{M-1}\sum_{q=0}^{Q-1}\int_{mT_r+qT_c+\tau-T_R}^{mT_r+(q+1)T_c} e^{j2\pi f_d t}dt + \int_{mT_r+(q+1)T_c}^{mT_r+(q+1)T_c+\tau-T_R} e^{j\psi_{mq}}e^{-j\psi_{m,q+1}}e^{j2\pi f_d t}dt. \quad (3.24)$$

Examining each integral separately, the first integral solution is

$$\frac{1}{j2\pi f_d}e^{j2\pi f_d}\Big|_{mT_r+qT_c+\tau-T_R}^{mT_r+(q+1)T_c} \quad (3.25)$$

Evaluating this solution with the limits of integration results in

$$\frac{1}{j2\pi f_d}\left[e^{j2\pi f_d(mT_r+(q+1)T_c)} - e^{j2\pi f_d(mT_r+qT_c+\tau-T_R)}\right] \quad (3.26)$$

Pulling out the common terms within the expression leaves

$$e^{j2\pi f_d mT_r}\frac{1}{j2\pi f_d}e^{j2\pi f_d qT_c}\left[e^{j2\pi f_d T_c} - e^{j2\pi f_d(\tau-T_R)}\right] \quad (3.27)$$

Just like the less than case, the exponential term containing the mT_R is pulled out in front of the Q summation. Pulling the $\tau - T_R$ term out of the brackets,

$$\frac{1}{j2\pi f_d}e^{j2\pi f_d(qT_c+\tau-T_R)}\left[e^{j2\pi f_d(T_c-\tau+T_R)} - 1\right], \quad (3.28)$$

allows for mathematical simplification later in the derivation. In an effort to get the bracketed terms into a form that resembles Euler's identity, the equation is reworked giving

$$\frac{e^{j2\pi f_d(qT_c+\tau-T_R)}}{j2\pi f_d}e^{j\pi f_d(T_c-\tau+T_R)}\left[e^{j\pi f_d(T_c-\tau+T_R)}-e^{-j\pi f_d(T_c-\tau+T_R)}\right] \tag{3.29}$$

The numerator and the denominator by $(T_c-\tau+T_R)$, completing Euler's identity. This reduction allows the equation to reduce to

$$(T_c-\tau+T_R)e^{j2\pi f_d(qT_c+\tau-T_R)}e^{j\pi f_d(T_c-\tau+T_R)}\text{sinc}[f_d(T_c-\tau+T_R)] \tag{3.30}$$

Now that the solution to the first integral is obtained, the second integral needs to be solved. The solution to the second integral is

$$e^{j(\psi_{mq}-\psi_{m,q+1})}\frac{1}{j2\pi f_d}e^{j2\pi f_d t}\Bigg|_{mT_r+(q+1)T_c}^{mT_r+(q+1)T_c+\tau-T_R} \tag{3.31}$$

Evaluating the solution with the limits of integration, the expression becomes

$$e^{j(\psi_{mq}-\psi_{m,q+1})}\frac{1}{j2\pi f_d}\left[e^{j2\pi f_d(mT_r+(q+1)T_c+\tau-T_R)}-e^{j2\pi f_d(mT_r+(q+1)T_c)}\right] \tag{3.32}$$

Pulling out the common terms from the expression gives

$$e^{j2\pi f_d mT_r}e^{j(\psi_{mq}-\psi_{m,q+1})}\frac{1}{j2\pi f_d}e^{j2\pi f_d(q+1)T_c}\left[e^{j2\pi f_d(\tau-T_R)}-1\right] \tag{3.33}$$

The term containing mT_r is pulled out ahead of the Q summation due to it being folded into the steering vector $\mathbf{b}(\bar{\omega})$

$$e^{j(\psi_{mq}-\psi_{m,q+1})}\frac{1}{j2\pi f_d}e^{j2\pi f_d(q+1)T_c}\left[e^{j2\pi f_d(\tau-T_R)}-1\right]. \tag{3.34}$$

Pulling an exponential out of the bracketed terms, the equation becomes

$$e^{j(\psi_{mq}-\psi_{m,q+1})}\frac{e^{j2\pi f_d(q+1)T_c}}{j2\pi f_d}e^{j\pi f_d(\tau-T_R)}\left[e^{j\pi f_d(\tau-T_R)}-e^{-j\pi f_d(\tau-T_R)}\right] \tag{3.35}$$

Multiplying the numerator and denominator by $\tau - T_R$ completes the expression to match Euler's identity. Therefore, the expression simplifies to

$$e^{j(\psi_{mq}-\psi_{m,q+1})}(\tau-T_R)e^{j2\pi f_d(q+1)T_c}e^{j\pi f_d\tau'}\text{sinc}[f_d(\tau-T_R)] \tag{3.36}$$

Therefore, combining (3.30) and (3.36) the overall expression for $0 < \tau - T_R < \frac{T_c}{2}$ is

$$\Phi(\tau-T_R>0,f_d)=\sum_{m=0}^{M-1}e^{j2\pi f_d mT_r}\sum_{q=0}^{Q-1}(T_c-\tau+T_R)(\tau-T_R)e^{j2\pi f_d(qT_c+\tau-T_R)}e^{j\pi f_d(T_c-\tau+T_R)}$$
$$\text{sinc}[f_d(T_c-\tau+T_R)]e^{j(\psi_{mq}-\psi_{m,q+1})}e^{j2\pi f_d(q+1)T_c}e^{j\pi f_d\tau'}\text{sinc}[f_d(\tau-T_R)] \tag{3.37}$$

3.2.3 Equal to Case ($\tau - T_R = 0$). The same development method is followed for this case. However, the pulses are perfectly matched. Perfectly matched implies that the phases of each chip cancel each other out and that $\tau = T_R$ as seen in Fig 3.3. Therefore, this TFACF becomes

$$\Phi(\tau=T_R,f_d)=\int_0^T e^{j2\pi f_d t}dt. \tag{3.38}$$

Since the energy is normalized to one, this equation is just a Fourier Transform of a rect function over the interval of T. Therefore, the expression of the TFACF for the equal to case is simply [6]

$$\Phi(\tau=T_R,f_d)=T\text{sinc}(f_dT). \tag{3.39}$$

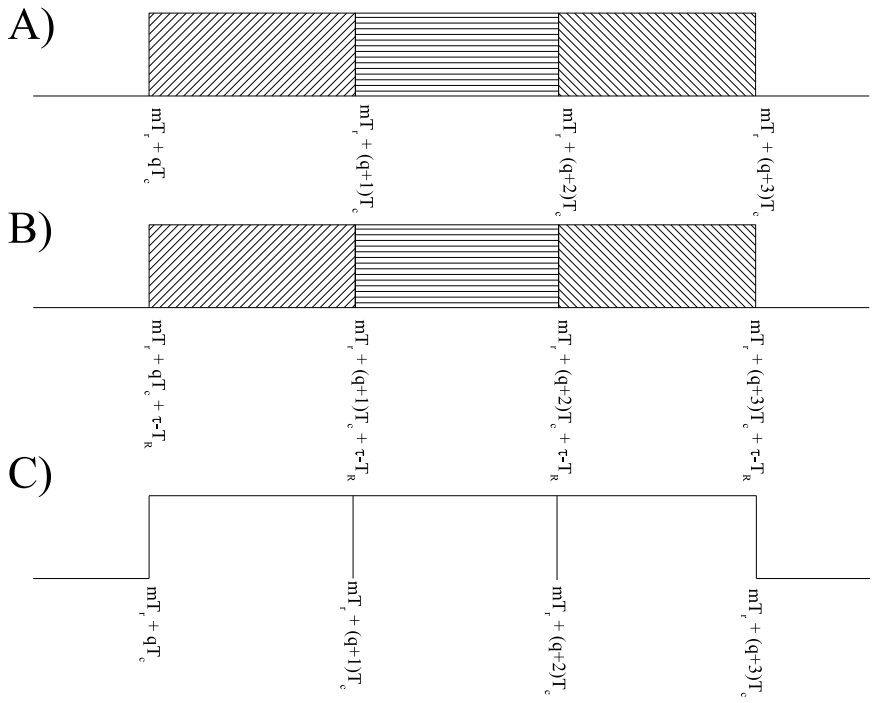

Figure 3.3: This case occurs when the pulses are perfectly matched.

All three cases (less than, greater than, and equal to) are required to be evaluated depending on the location of $\tau - T_R$ within the clutter ring, where $|\tau - T_R| \leq \frac{T_c}{2}$.

3.3 Linear Frequency Modulation

Creating the expression for the TFACF of the Linear Frequency Modulation (LFM) waveform requires different mathematics. This requirement is because LFM is not a discrete waveform like the other pulse compression waveform techniques. Other techniques like a Barker code or a Gold code change the phase from chip to chip. LFM is a frequency ramp and therefore contains no chips within the pulse.

Just like the generic case with dependance on chips, LFM has three different cases requiring examination for matching up pulses. However, due to the continuous nature of the LFM waveform, the transmitted LFM form is different. The new transmitted waveform is

$$s(t) = \sum_{m=0}^{M-1} u(t - mT_r) e^{j2\pi\alpha(t-mT_r)^2} \tag{3.40}$$

where α is the chirp rate. Therefore, the TFACF expression becomes

$$\Phi(\tau, f_d) = \sum_{m=0}^{M-1} \sum_{y=0}^{M-1} \int_{-\infty}^{\infty} u(t - mT_r) e^{j2\pi\alpha(t-mT_r)^2} u(t - yT_r - \tau - T_R) \\ e^{-j2\pi\alpha(t-mT_r-\tau-T_R)^2} e^{j2\pi f_d t} dt \tag{3.41}$$

where y is number of the returned pulse.

At this point, an assumption is made that $T_r > 2T$. This ensures the transmitted pulse matches with only one other returned pulse. If this assumption does not hold, then multiple pulse overlap may occur.

3.3.1 Less Than Case ($\tau - T_R < 0$). This case is when the received pulse is early as seen in Fig 3.4. The LFM case is more difficult to determine the limits

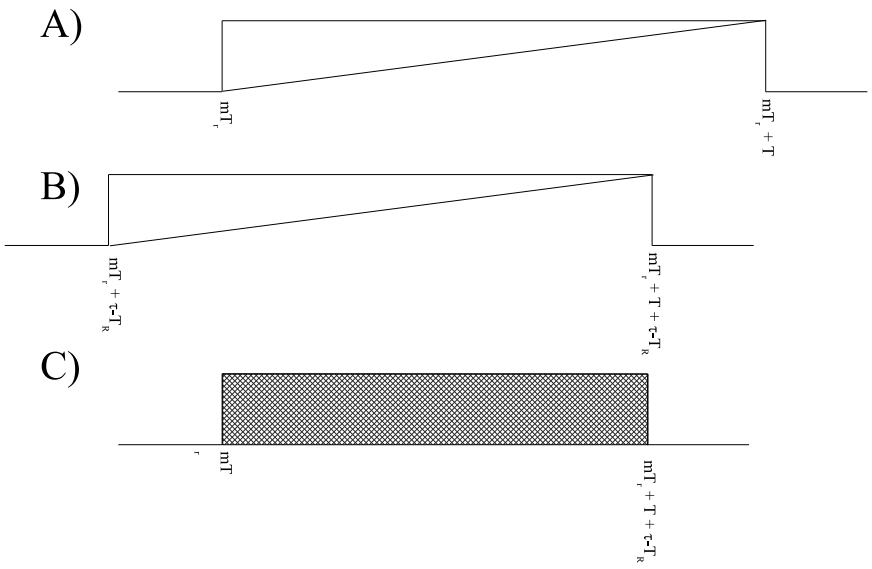

Figure 3.4: This LFM case occurs when the received pulse is early. A frequency mismatch occurs which effects the TFACF.

of integration. Multiple pulses are required before a clear picture is gained. For the less than case, the lower limit is mT_r while the upper limit is $mT_r + T + \tau - T_R$

$$\Phi(\tau - T_R < 0, f_d) = \sum_{m=0}^{M-1} \int_{mT_r}^{mT_r+T+\tau-T_R} e^{j2\pi\alpha(t-mT_r)^2} e^{-j2\pi\alpha(t-mT_r-\tau-T_R)^2} e^{j2\pi f_d t} dt. \tag{3.42}$$

The first step is to expand the exponentials. This expansion of the exponentials,

$$\int_{mT_r}^{mT_r+T+\tau-T_R} e^{j2\pi\alpha(t^2-2tmT_r+mT_r^2)} \\ e^{-j2\pi\alpha(t^2-2tmT_r-2t\tau-T_R+mT_r^2+2\tau-T_RmT_r+(\tau-T_R)^2)} e^{j2\pi f_d t} dt, \tag{3.43}$$

allows for simplification of the integral. Cancelation of like terms in the exponentials reduces the expression to

$$\int_{mT_r}^{mT_r+T+\tau-T_R} e^{-j2\pi\alpha(-2t\tau-T_R+2\tau-T_RmT_r+(\tau-T_R)^2)} e^{j2\pi f_d t} dt. \tag{3.44}$$

Pulling terms not dependant on t out of the integral gives

$$e^{-j2\pi\alpha(2\tau-T_R mT_r+(\tau-T_R)^2)}\int_{mT_r}^{mT_r+T+\tau-T_R} e^{-j2\pi\alpha(-2t\tau-T_R+f_d)t}dt. \tag{3.45}$$

The solution to the integral is

$$e^{-j2\pi\alpha(2\tau-T_R mT_r+(\tau-T_R)^2)}\frac{1}{j2\pi\alpha(2\tau-T_R-f_d)}e^{-j2\pi\alpha(-2t\tau-T_R+f_d)t}\Big|_{mT_r}^{mT_r+T+\tau-T_R} \tag{3.46}$$

An evaluation of the solution at the limits of integration results in

$$e^{-j2\pi\alpha(2\tau-T_R mT_r+(\tau-T_R)^2)}\frac{1}{j2\pi\alpha(2\tau-T_R-f_d)} \left[e^{j2\pi\alpha(2\tau-T_R-f_d)(mT_r+T+\tau-T_R)}-e^{j2\pi\alpha(2\tau-T_R-f_d)mT_r}\right] \tag{3.47}$$

Pulling the common terms out of the bracket gives

$$e^{-j2\pi\alpha(2\tau-T_R mT_r+(\tau-T_R)^2)}\frac{1}{j2\pi\alpha(2\tau-T_R-f_d)} e^{j2\pi\alpha(2\tau-T_R-f_d)mT_r}\left[e^{j2\pi\alpha(2\tau-T_R-f_d)(T+\tau-T_R)}-1\right] \tag{3.48}$$

Pulling out a exponential from the bracketed terms gives

$$e^{-j2\pi\alpha(2\tau-T_R mT_r+(\tau-T_R)^2)}\frac{1}{j2\pi\alpha(2\tau-T_R-f_d)}e^{j2\pi\alpha(2\tau-T_R-f_d)mT_r} e^{j\pi\alpha(2\tau-T_R-f_d)(T+\tau-T_R)}\left[e^{j\pi\alpha(2\tau-T_R-f_d)(T+\tau-T_R)}-e^{-j\pi\alpha(2\tau-T_R-f_d)(T+\tau-T_R)}\right] \tag{3.49}$$

Recognizing the expression as similar to Euler's identity, a multiplication of the numerator and denominator is needed. The equation is multiplied by $T-\tau-T_R$ to complete Euler's identity. Thus, providing the capability to rewrite the expression

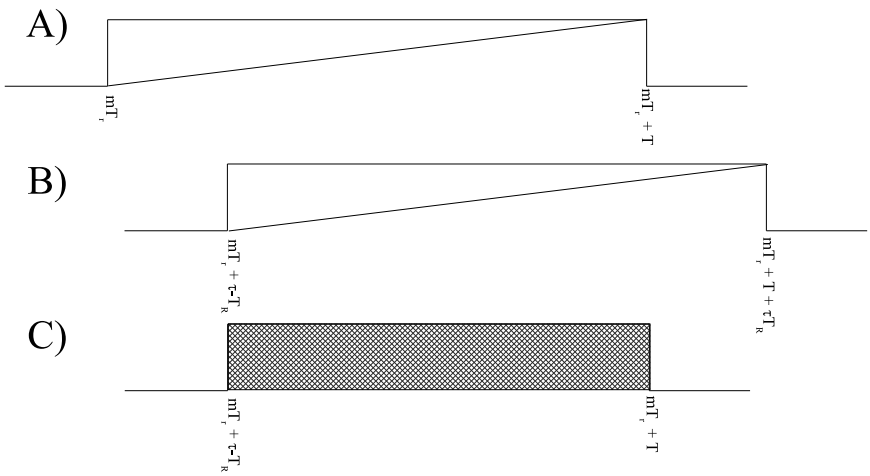

Figure 3.5: This LFM case occurs when the received signal arrives late. This creates a mismatch with the frequencies.

as

$$e^{j2\pi\alpha(-2\tau-T_R mT_r)}e^{-j2\pi\alpha(\tau-T_R)^2}e^{j2\pi mT_r[\alpha(2\tau-T_R-f_d)]}$$
$$e^{j\pi\alpha(2\tau-T_R-f_d)(T-\tau-T_R)}(T-\tau-T_R)\text{sinc}[\alpha(2\tau-T_R-f_d)(T+\tau-T_R)] \quad (3.50)$$

After simplification of the equation, the final expression for $-\frac{T_c}{2} < \tau - T_R < 0$ is

$$\Phi(\tau - T_R < 0, f_d) = \sum_{m=0}^{M-1} e^{-j2\pi mT_r f_d}e^{-j2\pi\alpha(\tau-T_R)^2}e^{j\pi\alpha(2\tau-T_R-f_d)(T-\tau-T_R)}$$
$$(T-\tau-T_R)\text{sinc}[\alpha(2\tau-T_R-f_d)(T+\tau-T_R)] \quad (3.51)$$

3.3.2 Greater Than Case ($\tau - T_R > 0$). This case occurs when the received pulse is late as seen in Fig 3.5. For the greater than case, the lower limit is $mT_r + \tau - T_R$ while the upper limit is $mT_r + T$,

$$\Phi(\tau - T_R > 0, f_d) = \sum_{m=0}^{M-1} \int_{mT_r+\tau-T_R}^{mT_r+T} e^{j2\pi\alpha(t-mT_r)^2}e^{-j2\pi\alpha(t-mT_r-\tau-T_R)^2}e^{j2\pi f_d t}dt. \quad (3.52)$$

Before solving the integral, an expansion of the exponentials,

$$\int_{mT_r+\tau-T_R}^{mT_r+T} e^{j2\pi\alpha(t^2-2tmT_r+mT_r^2)} e^{-j2\pi\alpha(t^2-2tmT_r-2t\tau-T_R+mT_r^2+2\tau-T_RmT_r+(\tau-T_R)^2)} e^{j2\pi f_d t} dt, \tag{3.53}$$

is completed to simplify the integral. Cancelation of like terms in the exponential reduces the expression to

$$\int_{mT_r+\tau-T_R}^{mT_r+T} e^{-j2\pi\alpha(-2t\tau-T_R+2\tau-T_RmT_r+(\tau-T_R)^2)} e^{j2\pi f_d t} dt. \tag{3.54}$$

Pulling the terms not dependant on t out from the integral gives

$$e^{-j2\pi\alpha(2\tau-T_RmT_r+(\tau-T_R)^2)} \int_{mT_r+\tau-T_R}^{mT_r+T} e^{-j2\pi\alpha(-2t\tau-T_R+f_d)t} dt. \tag{3.55}$$

The solution to the integral is

$$e^{-j2\pi\alpha(2\tau-T_RmT_r+(\tau-T_R)^2)} \frac{1}{j2\pi\alpha(2\tau-T_R-f_d)} e^{-j2\pi\alpha(-2t\tau-T_R+f_d)t} \Big|_{mT_r+T}^{mT_r+\tau-T_R}. \tag{3.56}$$

Evaluating the solution at the limits of integration gives

$$e^{-j2\pi\alpha(2\tau-T_RmT_r+(\tau-T_R)^2)} \frac{1}{j2\pi\alpha(2\tau-T_R-f_d)} \left[e^{j2\pi\alpha(2\tau-T_R-f_d)(mT_r+\tau-T_R)} - e^{j2\pi\alpha(2\tau-T_R-f_d)(mT_r+T)}\right]. \tag{3.57}$$

Pulling the common terms out from the bracketed terms results in

$$e^{-j2\pi\alpha(2\tau-T_RmT_r+(\tau-T_R)^2)} \frac{1}{j2\pi\alpha(2\tau-T_R-f_d)} e^{j2\pi\alpha(2\tau-T_R-f_d)(mT_r+\tau-T_R)} \left[e^{j2\pi\alpha(2\tau-T_R-f_d)(T-\tau-T_R)} - 1\right]. \tag{3.58}$$

Rewriting the equation after pulling out an exponential from the bracket terms gives

$$e^{-j2\pi\alpha(2\tau-T_R mT_r+(\tau-T_R)^2)}\frac{e^{j2\pi\alpha(2\tau-T_R-f_d)(mT_r+\tau-T_R)}}{j2\pi\alpha(2\tau-T_R-f_d)}$$
$$e^{j\pi\alpha(2\tau-T_R-f_d)(T-\tau-T_R)}\left[e^{j\pi\alpha(2\tau-T_R-f_d)(T-\tau-T_R)}-e^{-j\pi\alpha(2\tau-T_R-f_d)(T-\tau-T_R)}\right]. \quad (3.59)$$

Recognizing a form similar to Euler's identity, the numerator and denominator are multiplied by $T-\tau-T_R$,

$$e^{-j2\pi\alpha(2\tau-T_R mT_r+(\tau-T_R)^2)}e^{j2\pi\alpha(2\tau-T_R-f_d)(mT_r+\tau-T_R)}$$
$$e^{j\pi\alpha(2\tau-T_R-f_d)(T-\tau-T_R)}(T-\tau-T_R)\text{sinc}[\alpha(2\tau-T_R-f_d)(T-\tau-T_R)], \quad (3.60)$$

completing Euler's identity. Simplifying this equation to the final form,

$$e^{-j2\pi\alpha(\tau-T_R)^2}e^{j2\pi(2\alpha\tau-T_R+f_d)\tau-T_R}$$
$$e^{j\pi(2\alpha\tau-T_R+f_d)(T-\tau-T_R)}(T-\tau-T_R)\text{sinc}[\alpha(2\tau-T_R-f_d)(T-\tau-T_R)] \quad (3.61)$$

$$\sum_{m=0}^{M-1}e^{-j2\pi mT_r f_d}e^{-j2\pi\alpha(\tau-T_R)^2}e^{j\pi\alpha(2\tau-T_R-f_d)(T-\tau-T_R)}(T-\tau-T_R)\text{sinc}[\alpha(2\tau-T_R-f_d)(T+\tau-T_R)] \quad (3.62)$$

3.3.3 Equal to Case ($\tau - T_R = 0$). For the equal case, the pulses are perfectly matched. Therefore, $\tau - T_R = 0$ which makes the equation reduces to

$$\Phi(\tau = T_R, f_d) = \int_0^T e^{j2\pi f_d t}dt \quad (3.63)$$

Since the energy in the transmitted LFM is normalized to one, this equation is seen as a Fourier Transform of a rect function across duration T. Therefore, the expression

for the TFACF when $\tau = T_R$ is [6]

$$\Phi(\tau = T_R, f_d) = T\text{sinc}(f_d T) \tag{3.64}$$

At this point, all the derivations for this research have been completed. The next step is to simulate the derived TFACF's in $MATLAB$® and complete analysis.

IV. Results

Results from examining radar model effects due to removing the Doppler and range mismatch assumptions are provided this chapter. Incorporating a non-approximated value of the Time Frequency Auto Correlation Function (TFACF) into the model induces adverse effects on performance. An analysis is completed to evaluate the effects that the TFACF has on the model. This analysis is completed by comparing the conventional model to the results from the scaled model. The simple rectangular pulse was used to ensure that code used to model the TFACF was correctly completed. After the results are confirmed, several other waveforms are implemented, including 13-length Barker, 26-length concatenated Barker, two different Gold codes, Linear Frequency Modulated code, and two different sized Frank codes. Before the analysis begins, an understanding of the analysis tools is beneficial for drawing conclusions.

4.1 Analysis Tools

There are four different methods used to gain insight into the differences between the approximated model and the scaled model. These tools help to determine any performance variations that the radar model may incur by removing the TFACF approximation from the model. These techniques operate on the noise and interference covariance matrix built from the received signal, as outlined in Chapter 2.

4.1.1 Signal Match. The Signal Match (SM) technique, also known as the Fourier Spectra, determines a maximum whenever the steering vector matches a signal vector within the covariance matrix [4]. The SM technique determines the maximum by using the normalized power output, defined as

$$P_{sm} = \frac{\mathbf{v}^H \mathbf{R}\ \mathbf{v}}{\mathbf{v}^H \mathbf{v}}, \tag{4.1}$$

where $\mathbf{v}$ is the steering vector, H represents the hermitian operation, and $\mathbf{R}$ is the covariance matrix. This technique is a two-dimensional Fourier Transform, a uniform linear array and a radar having constant PRF [4]. The SM is a low resolution technique providing information on detection ability by showing the strength of the clutter returns.

Caution must be used when using this technique. A lack of resolution may introduce biased estimates when multiple signals are present which may cancel weaker signals [4]. A byproduct of the Fourier transform, the SM technique produces sidelobes which may hide the true clutter response.

This low resolution technique provides an accurate picture of the clutter spectrum, yet it is not reliable for accurate estimation of range resolution. To achieve an accurate resolution plot, a high resolution technique is needed, which provides the ability to distinguishing multiple targets.

4.1.2 Minimum Variance Estimator. The Minimum Variance (MV) estimator is considered a high resolution technique. MV output power is defined as

$$P_{MV} = (\mathbf{v}^H \mathbf{R}^{-1} \mathbf{v})^{-1}. \tag{4.2}$$

A primary difference between the MV and the SM is that the MV does not provide an accurate magnitude response, implying that the strength of the clutter returns is not accurate on these plots. What MV plots provide is the capability to distinguish multiple targets [4]. Higher range resolution allows for separation of targets that are located close together.

A substitution for the MV is the Maximum Entropy Method (MEM), which is also considered a high resolution technique. However, according to Klemm [4], the results from using the MEM are "quite 'spiky' and do not reflect the true spectrum properly. As will be shown...the MV estimator is more appropriate."

A combination of the low and high resolution techniques provide good insight into the characteristics of the clutter returns. However, a tool is needed to understand the difficulty of the clutter environment. This tool is the Eigenvalue decomposition.

4.1.3 Eigenvalue Decomposition. To determine how difficult the clutter environment is, an eigenvalue decomposition is performed. The eigenvalue decomposition simply isolates the eigenvalues of the covariance matrix. These values are then sorted in ascending order and plotted. Looking at a typical plot, the greater the number of eigenvalues with a value exceeding that of the noise floor, the tougher the clutter environment is. A tough clutter environment increases the chance that weaker target returns are masked by higher clutter returns.

The complete picture of how the TFACF effects the radar is almost formed. However, there is one more tool that is needed to help provide the complete picture.

4.1.4 Optimum Matched Filter Output SINR. The optimum matched filtered output Signal to Interference plus Noise Ratio (SINR) is a function of the noise, interference covariance matrix and the steering vector, $\mathbf{v}$ [2]. The optimum SINR is computed using

$$\mathrm{SINR}_{\mathrm{opt}} = \sigma^2 \xi_t \mathbf{v}^H \mathbf{R}^{-1} \mathbf{v} \tag{4.3}$$

where ξ_t is the per pulse Signal to Noise Ratio (SNR) and σ^2 is the noise power. This analysis shows the performance degradation that occurs within the SINR.

A side step is require to provide more insight into the SINR plots. The thermal noise power limit is determined using the best case power level if there was no clutter returned. The thermal noise power limit is given by

$$\sigma^2_{\mathrm{limit}} = \sigma^2 \xi_t \mathbf{v}^H \frac{1}{\sigma^2} \mathbf{I} \mathbf{v}, \tag{4.4}$$

which simplifies to

$$\sigma^2_{\mathrm{limit}} = \xi_t \mathbf{v}^H \mathbf{v}. \tag{4.5}$$

The model in this work assumes that $\xi_t = 1$. Therefore, (4.5) produces a vector of size MNP or $16 \times 16 \times 2 = 64$. Converting the values of this vector to decibels gives

$$10\log_{10}(MNP) = 10\log_{10}(16 \times 16 \times 2) = 27.09 \text{ dB}. \tag{4.6}$$

This states that with the physical radar configuration the system cannot achieve a better SINR than 27.09 dB, the thermal noise limit.

Therefore, knowing the thermal noise limit, a clearer understanding of the effects from the clutter environment is gained. Any variation below the thermal noise limit is directly related to clutter.

The techniques outlined above provide a complete picture of the clutter environment. This picture provides insight into effects from removing the TFACF approximation in the model.

4.2 Simple Rectangular Pulse

The baseline waveform is the rectangular sinusoidal pulse without any phase coding. This waveform will have no adverse effects due to Doppler or range shifting. Therefore, before any modeling with different waveforms is completed, the TFACF scaled model is compared against the current approximated model, ensuring an accurate model.

Analysis starts by looking at TFACF results. The TFACF model is based on the expressions derived in Chapter 3. Plotting the TFACF, a visual check is performed, confirming that the results from the derived TFACF model in Chapter 3 matches the proven TFACF plots. Examining Fig 4.1, the plot shows exactly what is expected, a rectangular correlated signal producing a triangle shape combined with the sinc function as seen in [5]. Therefore, confidence is gained with the derivation of the TFACF and that it is correctly modeled.

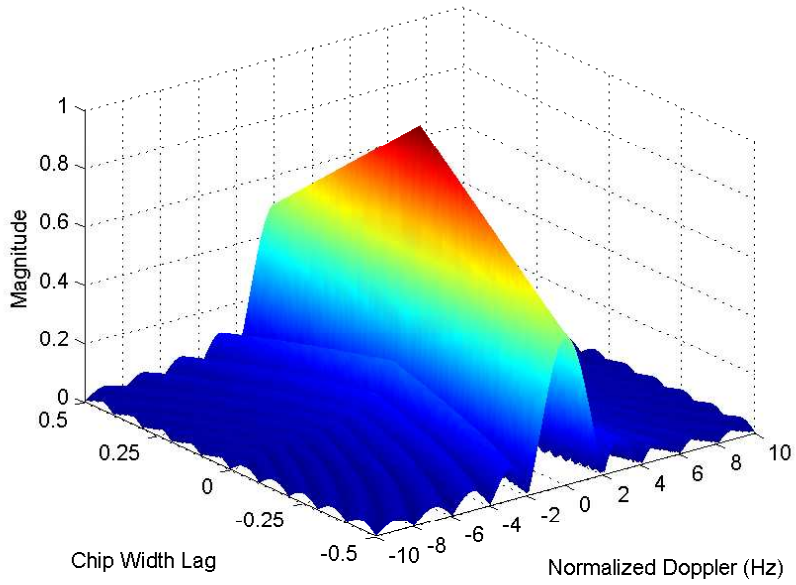

Figure 4.1: The Time Frequency Auto Correlation Function Plot of a simple rectangular pulse.

The first comparison made is that of the signal match technique. Plotted SM results for the simple rectangular case with no phase coding is seen in Fig 4.2 (a). As expected, the two signals from the approximated radar model and the TFACF scaled model are identical to each. This is due to no pulse compression techniques added to the signal which means there is no special phase coding structure with in the pulse. Therefore, any Doppler shift that has occurred will have no adverse effects on the TFACF model.

Examining the minimum variance estimator for the rectangular pulse, Fig 4.2 (b) shows the two different models plotted on top of each other. Again, this plot is expected. Since there is no phase coding within the pulse, the TFACF equals one. This makes the models identical. Hence the resolution curves are equal to each other.

The eigenvalue decomposition, Fig 4.2 (c), shows no difference between the two models. This is expected due to the lack of pulse compression technique. As stated

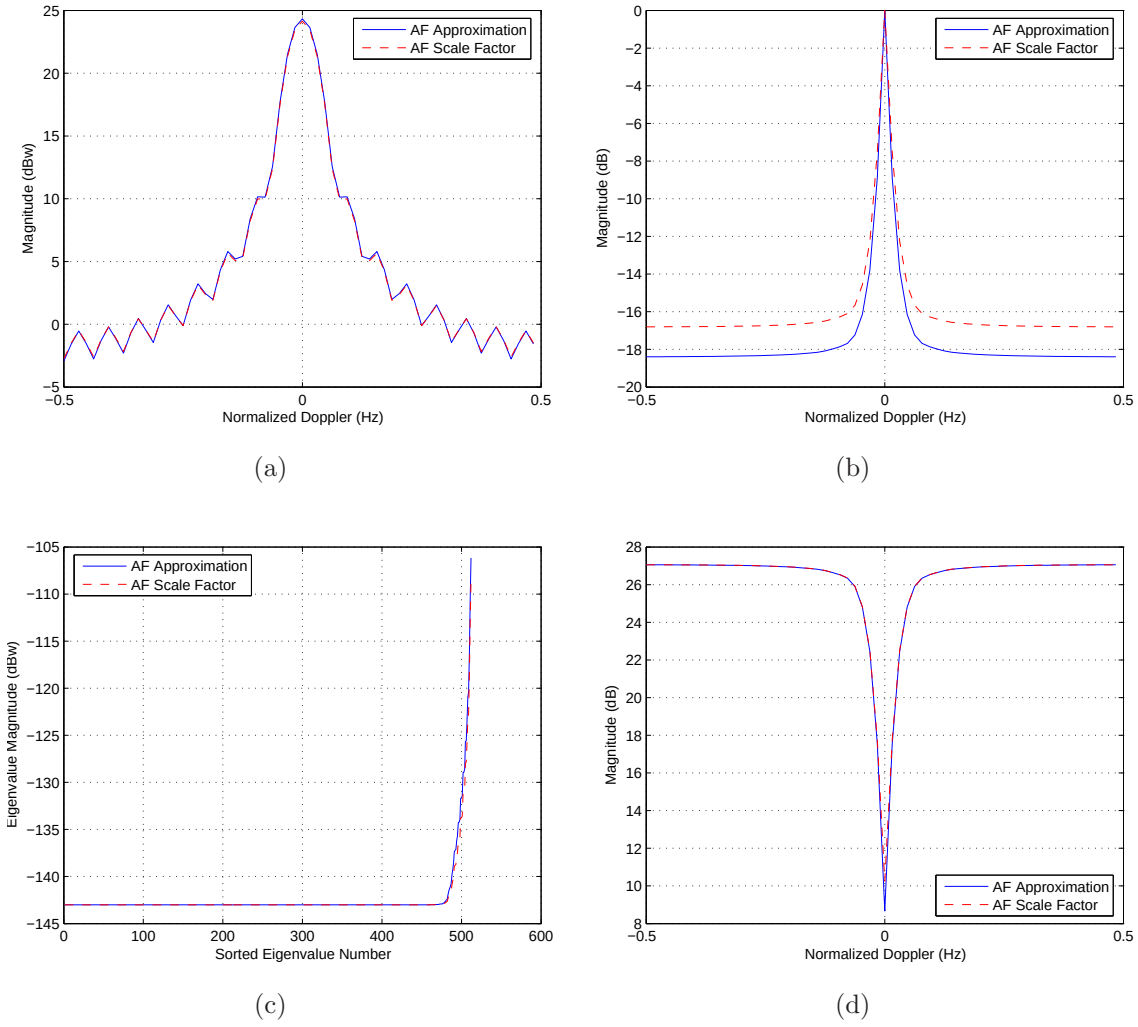

Figure 4.2: Unmodulated Rectangular Pulse
(a) Signal match describing the clutter spectrum.
(b) MVE describing the resolution capability utilizing this waveform.
(c) Eigenvalue decomposition illustrating the rank of the clutter spectrum and the overall difficulty of the problem.
(d) Output SINR of fully adaptive Space Time Adaptive Processing (STAP) illustrating target detection capability at all normalized Doppler frequencies.

above, each model is identical. Therefore, the eigenvalues in each covariance matrix of the model will have the same values.

The output SINR for the fully adaptive STAP technique, Fig 4.2 (d), shows no variance between the two models, as expected. However, the effects of clutter are shown now. Main beam clutter, located about 0 H_z, degrades the SINR level by nearly 20 dB.

With the baseline, simple rectangular pulse tested, it is shown that the scaled TFACF model is derived and simulated correctly. By duplicating and matching results achieved from the approximated model, confidence is gained that the scaled model is correct. Therefore, additional waveforms are next examined.

4.3 Barker Code

The Barker code is a phase coding scheme producing equally low sidelobe levels [5]. Using this code allows for better resolution along the range axis. The problem with the Barker code is that the maximum code length is limited mathematically to thirteen sub-phases. Typically, for pulse compression, a large code length is desired to increase the range resolution. The Barker coding scheme is examined as a starting reference point for basic pulse compression coding.

4.3.1 13-Length Barker Code. Before examining the performance characterization metrics obtained by implementing the Barker code into the model, the TFACF of a 13-length Barker code is plotted as a check. This check ensures that the TFACF correctly models the Barker code. The Barker code is 1111100110101 [5] and is coded as phase shifts within each chip of a transmitted pulse. The value of 1 is represented as $e^{j\pi}$ and 0 is expressed as e^{j0} or 0. Figure 4.3 confirms, by matching expected results, that the TFACF model built still holds true for the 13-length Barker code sequence. With more confidence gained in the TFACF model,

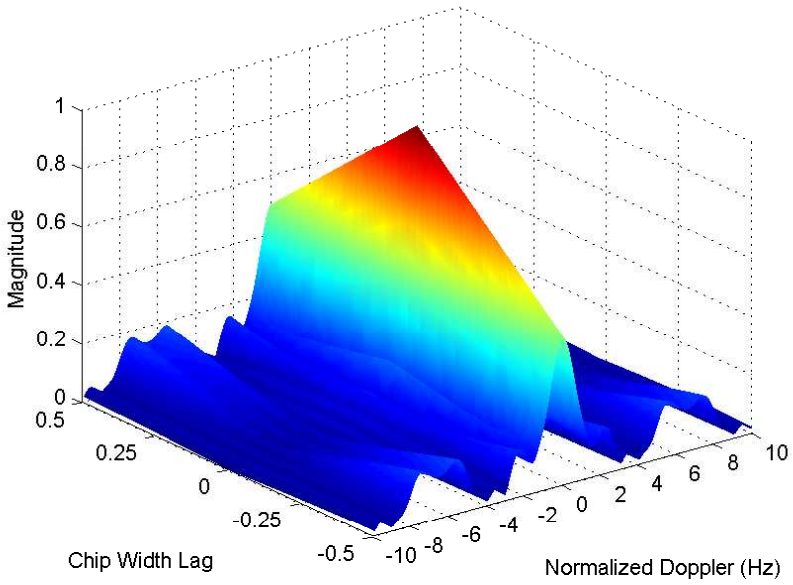

Figure 4.3: The Time Frequency Auto Correlation Function plot of the 13-Length Barker Coded pulse.

the comparison tools are implemented to gain insight to any performance trade-offs incurred.

Starting the comparison of the two models begins with the first technique, the SM. The results from the signal match are shown in Fig 4.4 (a). Immediately, a reduction of 3-dB of clutter power return is seen which indicates there is less clutter power entering the system.

The next step is to determine the resolution capability with the Barker code. Resolution capabilities is shown using the minimum variance estimator technique. The results from completing the MVE is shown in Fig 4.4 (b). The TFACF scaled factor return is not as sharp when compared to the approximated TFACF. This gain in width indicates that the resolution capability is degraded due to adding the scale factor.

The difficulty of the clutter problem is shown by eigenvalue decomposition, seen in Fig 4.4 (c). According to the plot, the scaled factor is affected more by

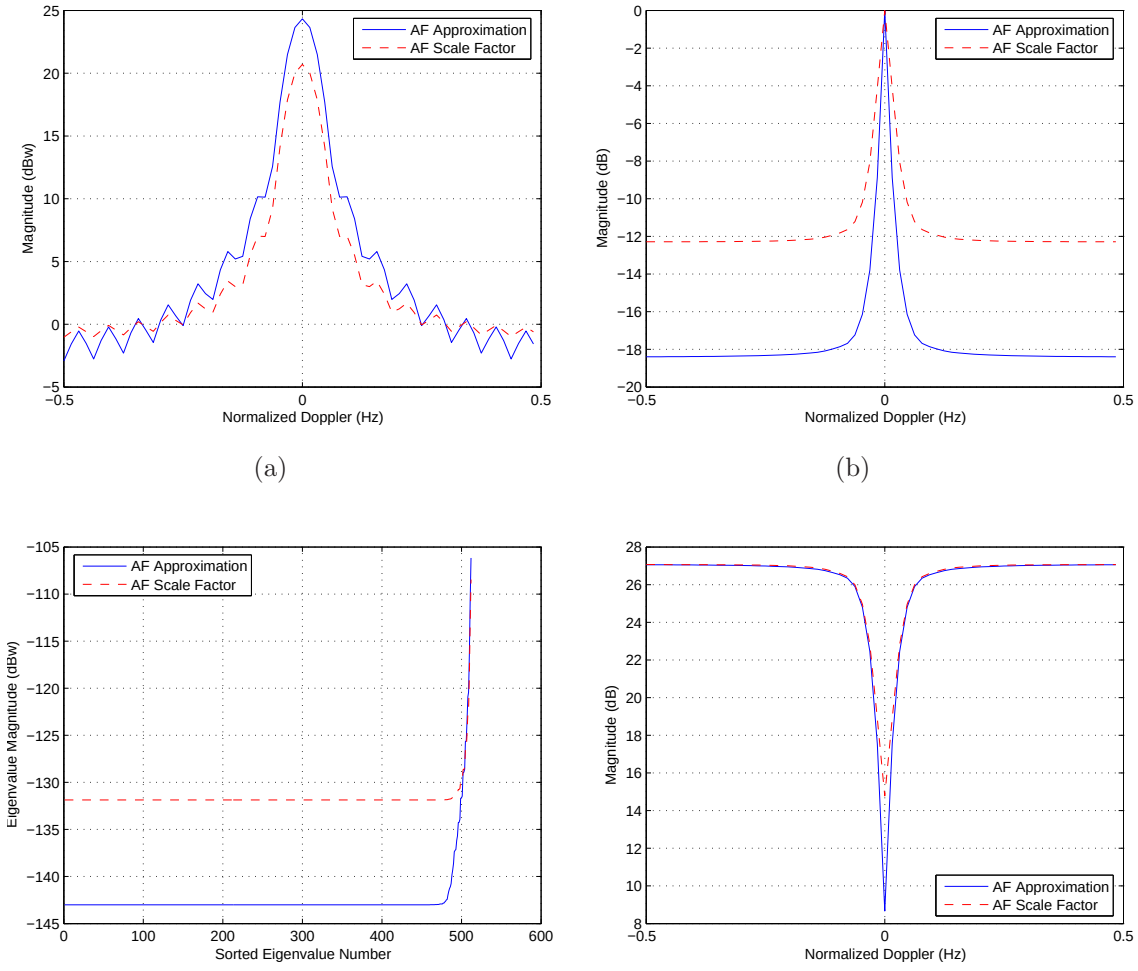

Figure 4.4: 13-Length Barker Coded Pulse
(a) Signal match describing the clutter spectrum.
(b) MVE describing the resolution capability utilizing this waveform.
(c) Eigenvalue decomposition illustrating the rank of the clutter spectrum and the overall difficulty of the problem.
(d) Output SINR of fully adaptive Space Time Adaptive Processing (STAP) illustrating target detection capability at all normalized Doppler frequencies.

thermal noise. The approximated TFACF noise floor is -143.5 dB while the scaled factor TFACF is around 131.5 dB. This difference in thermal noise is due to the change in bandwidth. The uncompressed bandwidth of the radar is defined as

$$B = \frac{1}{T} = 1.25 \text{ MH}_\text{z}. \tag{4.7}$$

Pulse compression effectively increases the bandwidth by dividing T into equal duration subpulses by the number or the code length. In this case, the code length is 13 long. Therefore, the compressed pulse width is $\frac{T}{13}$. This makes the new compressed bandwidth to be

$$B_c = \frac{13}{T} = 16.25 \text{ MH}_\text{z} \tag{4.8}$$

which is 15 MHz larger than the uncompressed pulse width. Therefore, a high thermal noise level. This increase in thermal noise dominates more of the clutter returns creating an easier clutter problem.

Examining Fig 4.4 (d), the optimum SINR values are shown. As mentioned above, main beam clutter drastically effects the output SINR of fully adaptive STAP. However, by increasing the bandwidth, 6 dB SINR improvement is gained.

4.3.2 26-Length Concatenated Barker Code. In an effort to harness the benefits of the Barker code, yet create a longer pulse than the original 13-length Barker code, a concatenated 26-length Barker code was created. Creating this concatenated code was accomplished by taking the original 13-length code and attaching a flipped version of the original code which results in 11111001101011010110011111. Again, the 1 is coded as $e^{j\pi}$ and 0 is coded as 0. The TFACF of this concatenated code is seen in Fig 4.5.

Changing from the 13-length Barker the 26-length concatenated code effects the returned clutter power as seen in Fig 4.6 (a). The clutter power is reduced 7 dB and a difference of 2 dB is seen between the two different Barker codes. This

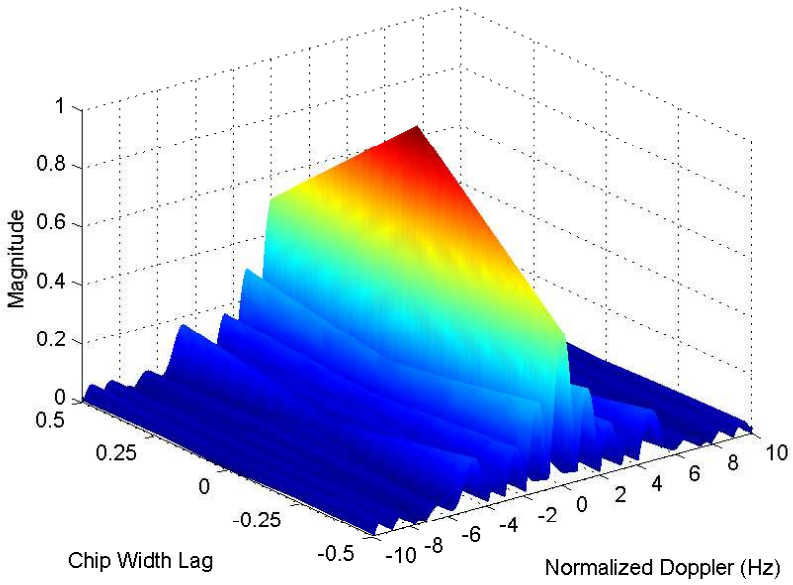

Figure 4.5: The Time Frequency Auto Correlation Function Plot of the 26-Length Concatenated Barker Coded pulse.

difference shows that as the length of the code increases, the signal strength from the clutter return slowly degrades.

The resolution capability of the concatenated Barker code shown in Fig. 4.6 (b) remains wider than that of the approximated model. Comparing the 26-length to that of the 13-length, a change in resolution is negligible. The only difference in the plots is that the floor of the scale factor TFACF increases by 1 dB.

The new bandwidth from the 26-length concatenated Barker code is

$$B_c = \frac{26}{T} = 32.5 \text{ MH}_\text{z}. \tag{4.9}$$

The compressed pulse bandwidth has increased by almost 30 MH_z. The eigenvalue decomposition shows in Fig. 4.6 that with the larger bandwidth of the concatenated pulse, the noise floor has risen to 129 dB, effectively making the clutter environment

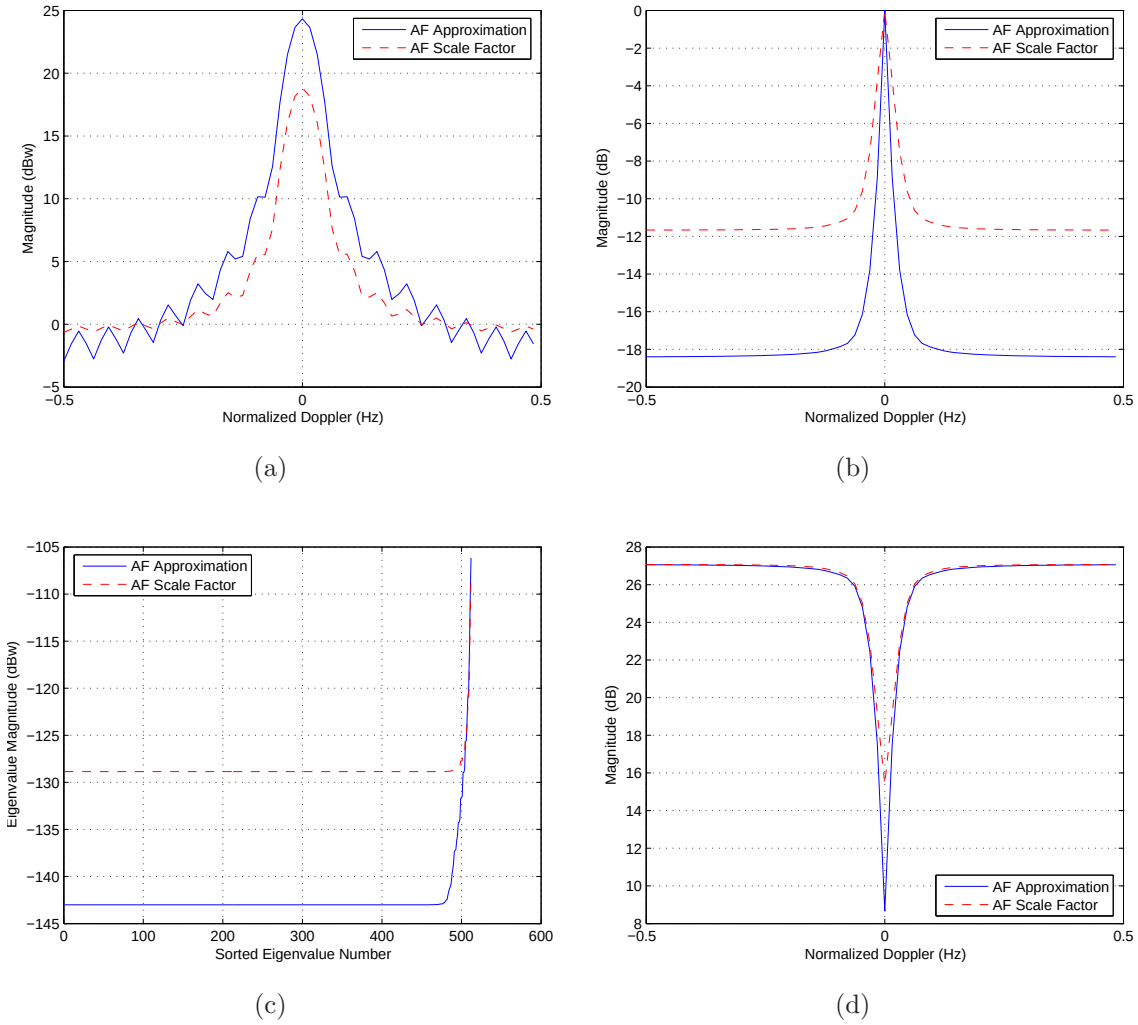

Figure 4.6: 26-Length Concatenated Barker Coded Pulse
(a) Signal match describing the clutter spectrum.
(b) MVE describing the resolution capability utilizing this waveform.
(c) Eigenvalue decomposition illustrating the rank of the clutter spectrum and the overall difficulty of the problem.
(d) Output SINR of fully adaptive Space Time Adaptive Processing (STAP) illustrating target detection capability at all normalized Doppler frequencies.

less difficult. Comparing the two Barker code TFACF, the concatenated Barker's noise floor increased 3 dB.

The optimized SINR output plot, Fig. 4.6 (d), shows a 8 dB gain. This gain is due to less clutter power returned. Comparing the difference between the two Barker codes, the concatenated code has a 2 dB greater SINR.

4.4 Frank Code

The Frank code is considered a polyphase code. A polyphase code occurs when the pulse compression need is not restricted to the binary coding level of 0 and π [5]. A Frank code is a $M \times M$ matrix where the first column is zeros while the rest of the values are found by taking the number of each row of the matrix (counting up from zero to $M-1$) and multiplying by a phase of $\frac{2\pi}{M}$ radians or $\frac{360}{M}$ degrees. A reorganization of this matrix for transmission results in a $1 \times M^2$ vector. Therefore, a single uncompressed pulse transmission looks like a transmission of M^2 pulses.

4.4.1 5-Length Frank Code. The first Frank code examined is the 5-length Frank code. As described above, the length of the actual transmit pulse is 5^2 or 25 subpulses. The phases are incremented in

$$\frac{2\pi}{M} = \frac{2\pi}{5} = 1.2566 \text{ radians} \tag{4.10}$$

or

$$\frac{360^o}{M} = \frac{360^o}{5} = 72^o. \tag{4.11}$$

Therefore, the matrix for the Frank code for $M = 5$ is

$$\begin{bmatrix} 0 & 0 & 0 & 0 & 0 \\ 0 & 1.2566 & 2.5133 & 3.7699 & 5.0265 \\ 0 & 2.5133 & 5.0265 & 1.2566 & 3.7699 \\ 0 & 3.7699 & 1.2566 & 5.0265 & 2.5133 \\ 0 & 5.0265 & 3.7699 & 2.5133 & 1.2566 \end{bmatrix} \tag{4.12}$$

where the numbers are in units of radians or

$$\begin{bmatrix} 0 & 0 & 0 & 0 & 0 \\ 0 & 72 & 144 & 216 & 288 \\ 0 & 144 & 288 & 72 & 216 \\ 0 & 216 & 72 & 288 & 144 \\ 0 & 288 & 216 & 144 & 72 \end{bmatrix} \tag{4.13}$$

where the numbers have units of degrees.

Since this is a polyphase code, the sidelobe levels are lower than a typical binary code and the code tends to be more Doppler tolerant. The TFACF for this code is shown in Fig 4.7. This plot depicts a typical Frank code showing lower sidelobe levels in the outlying regions.

Beginning the analysis, the signal match comparison in Fig 4.8 (a) is examined. A 6 dB degradation in clutter power is achieved with this Frank code. Comparing this plot to that of the concatenated Barker plots, similarities are seen. The magnitude and overall spectrum appear as almost identical plots. Fig 4.8 (b) shows the comparison using the MVE technique. Again, it is seen that the approximated resolution is better than the scaled model. Comparison of this Frank code to that of the concatenated Barker show negligible differences. A picture is starting to form that the major effect on the model is that of increased bandwidth, allowing for greater influence from thermal noise.

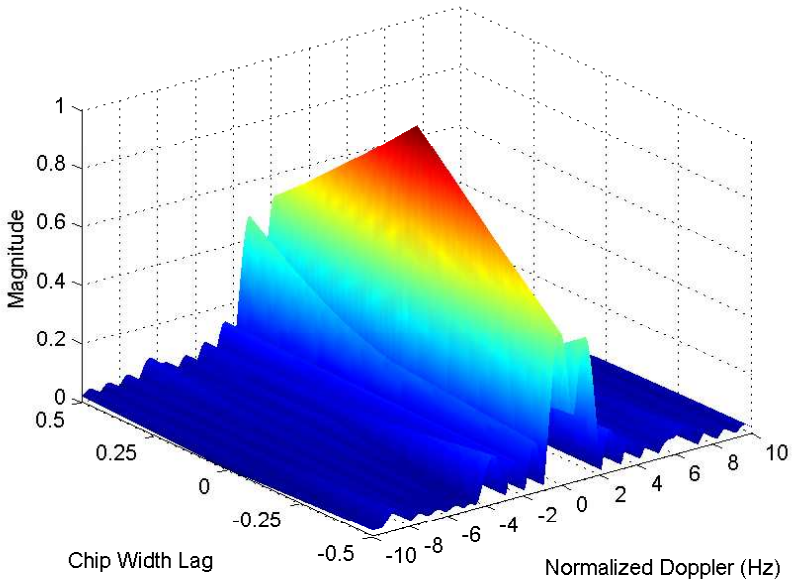

Figure 4.7: The Time Frequency Auto Correlation Function Plot of the 5-Length Frank Coded pulse.

The compressed bandwidth of this Frank code is

$$B_c = \frac{25}{T} = 31.25 \text{ MH}_\text{z}. \tag{4.14}$$

This is a difference of 30 MH_z from the uncompressed bandwidth. This difference is seen in the eigenvalue decomposition Fig 4.8 (c). This plot shows a noise floor of 129 dB which is equal to that of the concatenated Barker pulse. This correlation is starting to show that the larger the bandwidth, the easier clutter environment the radar deals with since the noise floor dominates many of the clutter returns.

Examining the output SINR of fully adaptive STAP, Fig 4.8 (d), a 7 dB gain is achieved by implementing the Frank code. This improvement is due to the smaller clutter power returns as seen in the SM plots. Again, a comparison of the Frank code results to that of the concatenated Barker are virtually the same plot suggesting that the biggest factor effecting the model is an increase in thermal noise power.

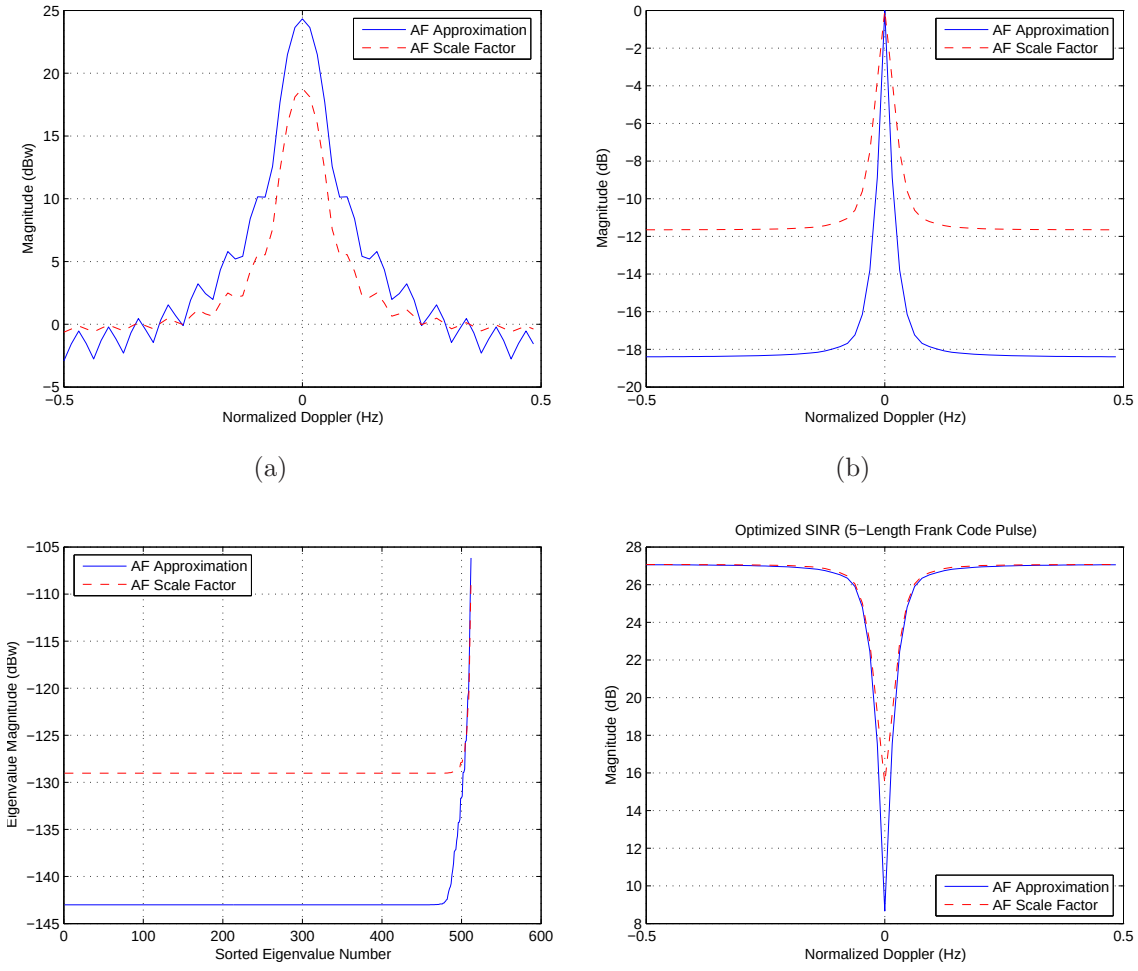

Figure 4.8: 5-Length Frank Coded Pulse
(a) Signal match describing the clutter spectrum.
(b) MVE describing the resolution capability utilizing this waveform.
(c) Eigenvalue decomposition illustrating the rank of the clutter spectrum and the overall difficulty of the problem.
(d) Output SINR of fully adaptive Space Time Adaptive Processing (STAP) illustrating target detection capability at all normalized Doppler frequencies.

4.4.2 10-Length Frank Code. The second Frank code examined is the 10-length Frank code. As described above, the length of the actual transmit pulse is 10^2 or 100 subpulses. The phases are incremented in

$$\frac{2\pi}{M} = \frac{2\pi}{10} = 0.6283 \text{ radians} \tag{4.15}$$

or

$$\frac{360^o}{M} = \frac{360^o}{10} = 360^o. \tag{4.16}$$

Therefore, the matrix for the Frank code with $M = 10$ is

$$\begin{bmatrix}
0 & 0 & 0 & 0 & 0 & 0 & 0 & 0 & 0 & 0 \\
0 & 0.6283 & 1.2566 & 1.8850 & 2.5133 & 3.1416 & 3.7699 & 4.3982 & 5.0265 & 5.6549 \\
0 & 1.2566 & 2.5133 & 3.7699 & 5.0265 & 0 & 1.2566 & 2.5133 & 3.7699 & 5.0265 \\
0 & 1.8850 & 3.7699 & 5.6549 & 1.2566 & 3.1416 & 5.0265 & 0.6283 & 2.5133 & 4.3982 \\
0 & 2.5133 & 5.0265 & 1.2566 & 3.7699 & 0 & 2.5133 & 5.0265 & 1.2566 & 3.7699 \\
0 & 3.1416 & 0 & 3.1416 & 0 & 3.1416 & 0 & 3.1416 & 0 & 3.1416 \\
0 & 3.7699 & 1.2566 & 5.0265 & 2.5133 & 0 & 3.7699 & 1.2566 & 5.0265 & 2.5133 \\
0 & 4.3982 & 2.5133 & 0.6283 & 5.0265 & 3.1416 & 1.2566 & 5.6549 & 3.7699 & 1.8850 \\
0 & 5.0265 & 3.7699 & 2.5133 & 1.2566 & 0 & 5.0265 & 3.7699 & 2.5133 & 1.2566 \\
0 & 5.6549 & 5.0265 & 4.3982 & 3.7699 & 3.1416 & 2.5133 & 1.8850 & 1.2566 & 0.6283
\end{bmatrix} \tag{4.17}$$

where the numbers are in units of radians or

$$\begin{bmatrix} 0 & 0 & 0 & 0 & 0 & 0 & 0 & 0 & 0 & 0 \\ 0 & 36 & 72 & 108 & 144 & 180 & 216 & 252 & 288 & 324 \\ 0 & 72 & 144 & 216 & 288 & 0 & 72 & 144 & 216 & 288 \\ 0 & 108 & 216 & 324 & 72 & 180 & 288 & 36 & 144 & 252 \\ 0 & 144 & 288 & 72 & 216 & 0 & 144 & 288 & 72 & 216 \\ 0 & 180 & 0 & 180 & 0 & 180 & 0 & 180 & 0 & 180 \\ 0 & 216 & 72 & 288 & 144 & 0 & 216 & 72 & 288 & 144 \\ 0 & 252 & 144 & 36 & 288 & 180 & 72 & 324 & 216 & 108 \\ 0 & 288 & 216 & 144 & 72 & 0 & 288 & 216 & 144 & 72 \\ 0 & 324 & 288 & 252 & 216 & 180 & 144 & 108 & 72 & 36 \end{bmatrix} \tag{4.18}$$

where the numbers have units of degrees.

Increasing the Frank code to a length 10 increases the length of the transmit codes to a length of 100. This increases the bandwidth while suppression of the sidelobes is greater than that of the 5-length Frank, as seen in Fig 4.9.

Figure 4.10 (a) shows the signal match metric for the 10-length Frank code. Implementing this compression scheme, return clutter power is reduced by 11 dB. This is the greatest hit seen thus far. However, this stands to reason due to the greatest increase in bandwidth.

The MVE plot, Fig 4.10 (b), shows that resolution is lost using this Frank code. The floor has risen to -10 dB and the beam has fattened, decreasing the resolution capability. When comparing against Fig 4.8 (b), the noise floor differs by 2 dB.

The compressed bandwidth for this case of the Frank code is

$$B_c = \frac{100}{T} = 125 \text{ MH}_\text{z}. \tag{4.19}$$

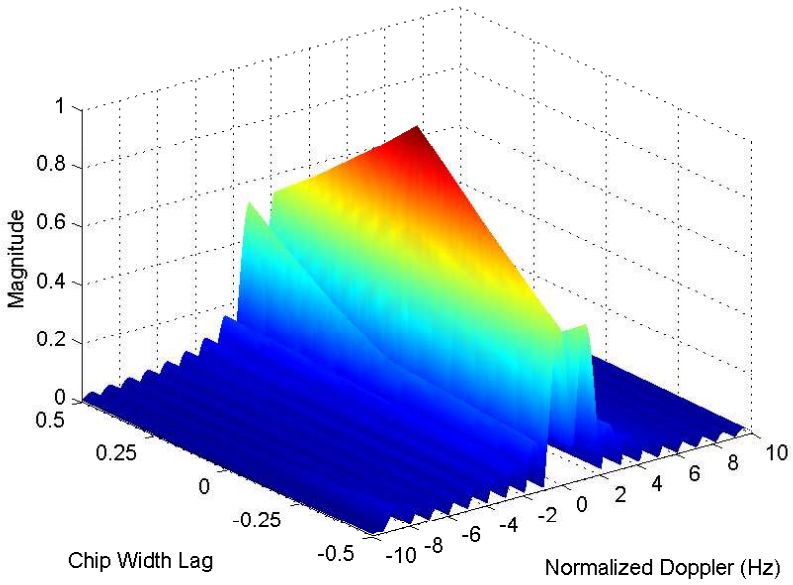

Figure 4.9: The Time Frequency Auto Correlation Function Plot of the 10-Length Frank Coded pulse.

This is increase in bandwidth by over 120MHz. Increasing the bandwidth greatly simplifies the clutter difficulty. This simplification is due to an increase the thermal noise level as seen in Fig 4.10 (c). This higher noise floor results in fewer clutter values being seen in the model.

By implementing the 10-length Frank code, the output SINR of a fully adaptive STAP process increased by 10 dB as seen in Fig. 4.10 (d). The SINR for the scaled factor TFACF is only 10 dB lower than that of the thermal noise limit, the level where the best SINR is achieved.

4.5 Gold Code

The next compression scheme examined is the Gold code. The Gold code has been shown to provide improvement with clutter suppression, unambiguous range properties and resolution [3]. Therefore, a 31-length Gold Code was implemented to see the effects, if any, on the TFACF scaled model.

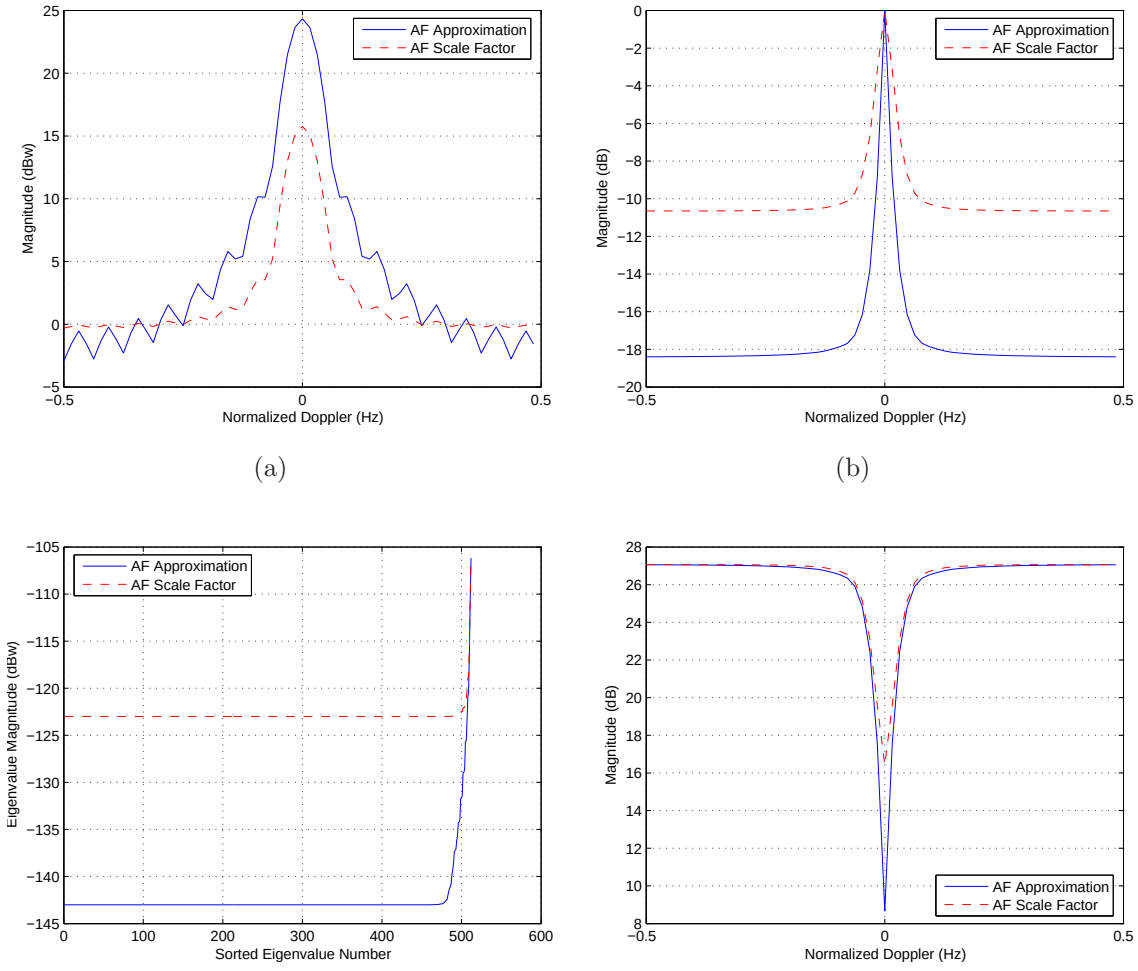

Figure 4.10: 10-Length Frank Coded Pulse
(a) Signal match describing the clutter spectrum.
(b) MVE describing the resolution capability utilizing this waveform.
(c) Eigenvalue decomposition illustrating the rank of the clutter spectrum and the overall difficulty of the problem.
(d) Output SINR of fully adaptive Space Time Adaptive Processing (STAP) illustrating target detection capability at all normalized Doppler frequencies.

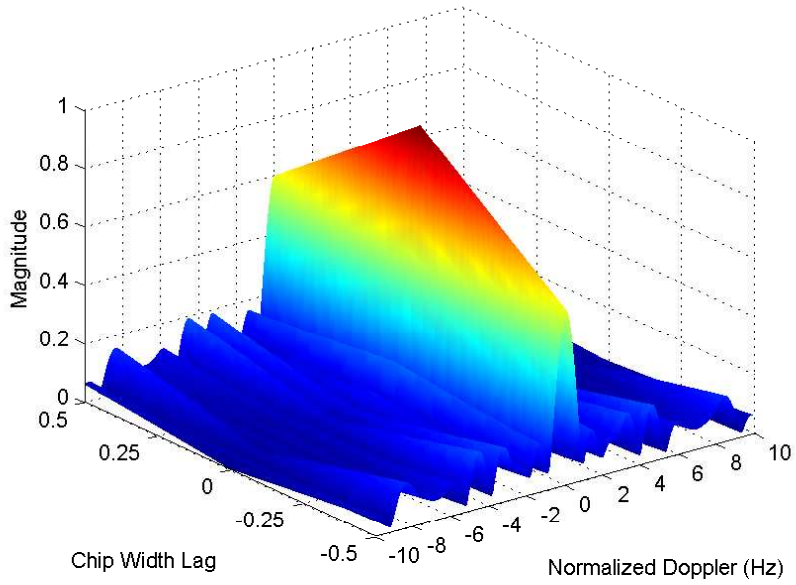

Figure 4.11: The Time Frequency Auto Correlation Function Plot of the First Gold Coded pulse.

4.5.1 First Gold Code. The first Gold code implemented is [3]

$$00011011110110100011111110100000. \tag{4.20}$$

For coding purposes, 1 is coded as a phase of $e^{j\pi}$ and 0 is coded as 0. Figure 4.11 shows the TFACF of the Gold code.

Referencing Fig 4.12 (a), the clutter spectrum of the gold code is plotted. Examining this plot, a 7 dB degradation of the clutter return power is gained by implementing this compression scheme.

The minimum variance plot of the gold code, Fig. 4.12 (b), indicates that resolution capabilities are lost by using a compressed pulse width.

Looking at the bandwidth of the Gold code,

$$B_c = \frac{31}{T} = 38.75 \text{ MH}_z, \tag{4.21}$$

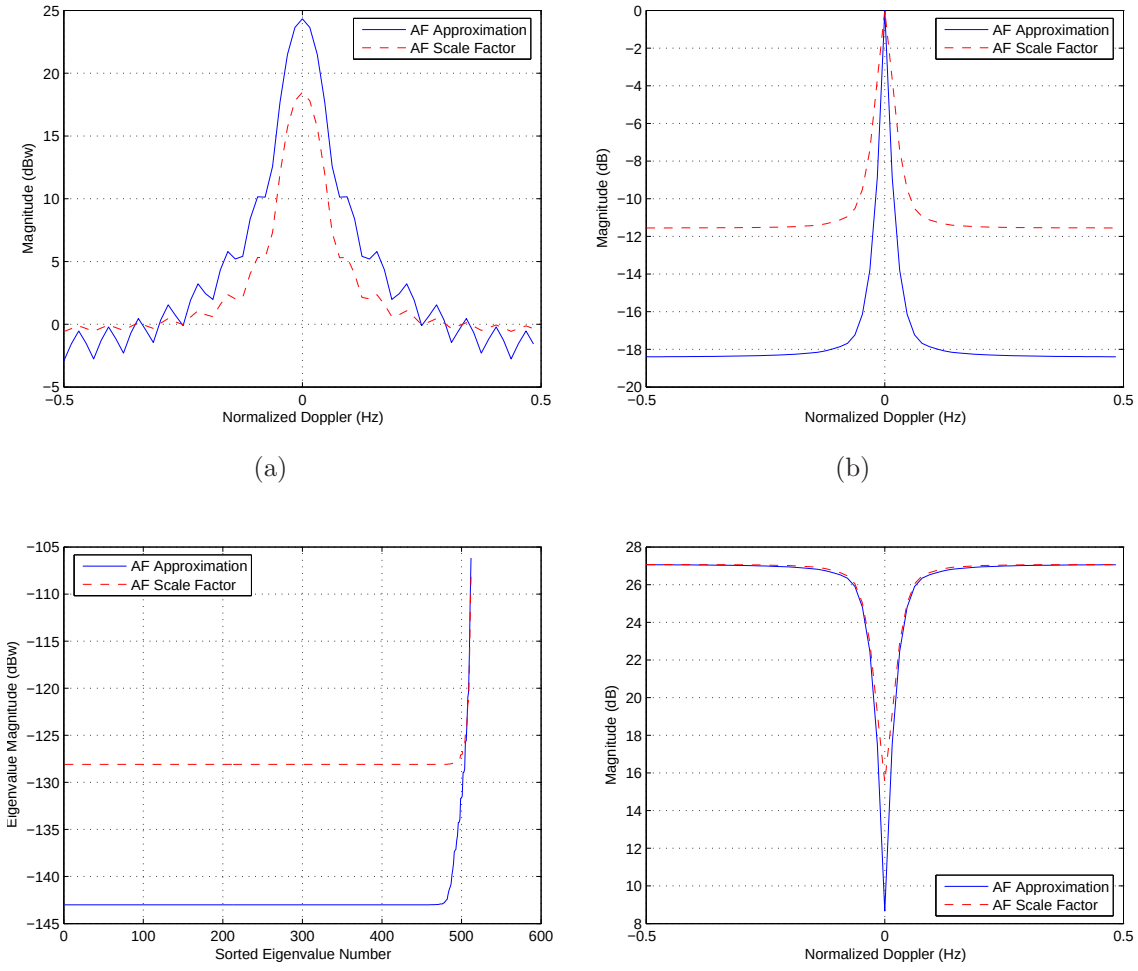

Figure 4.12: First Gold Coded Pulse
(a) Signal match describing the clutter spectrum.
(b) MVE describing the resolution capability utilizing this waveform.
(c) Eigenvalue decomposition illustrating the rank of the clutter spectrum and the overall difficulty of the problem.
(d) Output SINR of fully adaptive Space Time Adaptive Processing (STAP) illustrating target detection capability at all normalized Doppler frequencies.

an increase from the uncompress pulse bandwidth by more than 37 $\mathrm{MH_z}$ is found. Therefore, more thermal noise is introduced into the system. The eigenvalue decomposition shows this increase in thermal noise, Fig. 4.12 (c). The noise floor is at -127 dB which suppresses returns from the clutter environment, making the clutter problem easier than that scaled factor TFACF.

The output SINR of full adaptive STAP is increased by 8 dB as seen in Fig. 4.12 (d). This increase is due to less clutter power being returned which in turn decreases the main beam clutter return. The small main beam clutter return increases the best possible SINR close to the thermal noise limit.

4.5.2 Second Gold Code. The second Gold code is defined as [3]

$$0101100101100001001000000111010. \tag{4.22}$$

Again, this scheme is coded by using a binary phase scheme within the chips. A value of 1 is coded as $e^{j\pi}$ and 0 is coded as 0. Figure 4.13 shows the TFACF of the second Gold code.

Referencing Fig 4.14 (a), the clutter spectrum of the gold code is plotted. Examining this plot, a 7 dB degradation of the clutter return power is gained by implementing this compression scheme. This gain and plot is the same as the first Gold code. Any differences are minuet.

The minimum variance plot of the second gold code, Fig. 4.14 (b), indicates that resolution capabilities are lost by using a compressed pulse width. Comparing this plot against Fig. 4.12 (b), the resolution capability is very similar between each Gold code.

Examining the bandwidth of the second Gold code,

$$B_c = \frac{31}{T} = 38.75 \text{ MH}_\text{z}, \tag{4.23}$$

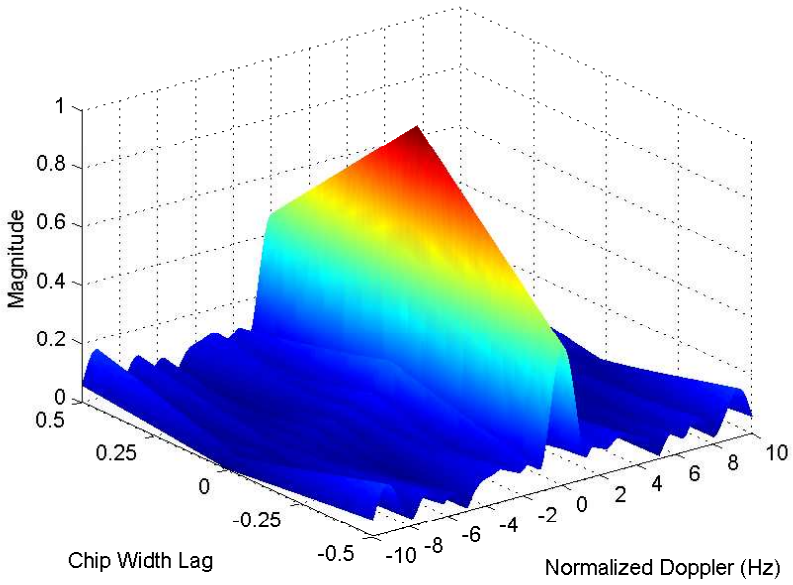

Figure 4.13: The Time Frequency Auto Correlation Function Plot of the Second Gold Coded pulse.

an increase from the uncompress pulse bandwidth by more than 37 MH_z is found. This bandwidth is identical to the first Gold code. However, equal bandwidths are expected since each code is a length of 31. Therefore, the thermal noise introduced into the system is identical to that of the first Gold code. The eigenvalue decomposition shows this increase in thermal noise, Fig. 4.14 (c).

The output SINR of full adaptive STAP is increased by 8 dB as seen in Fig. 4.14 (d). This increase is due to less clutter power being returned which in turn decreases the main beam clutter return. The small main beam clutter return increases the best possible SINR close to the thermal noise limit.

4.6 Linear Frequency Modulation Code

The last waveform examined is the Linear Frequency Modulation (LFM) code. This is the most common transmitted pulse and is frequently used with Synthetic Aperture Radar systems. As outlined in Chapter 3, the LFM is not discrete like

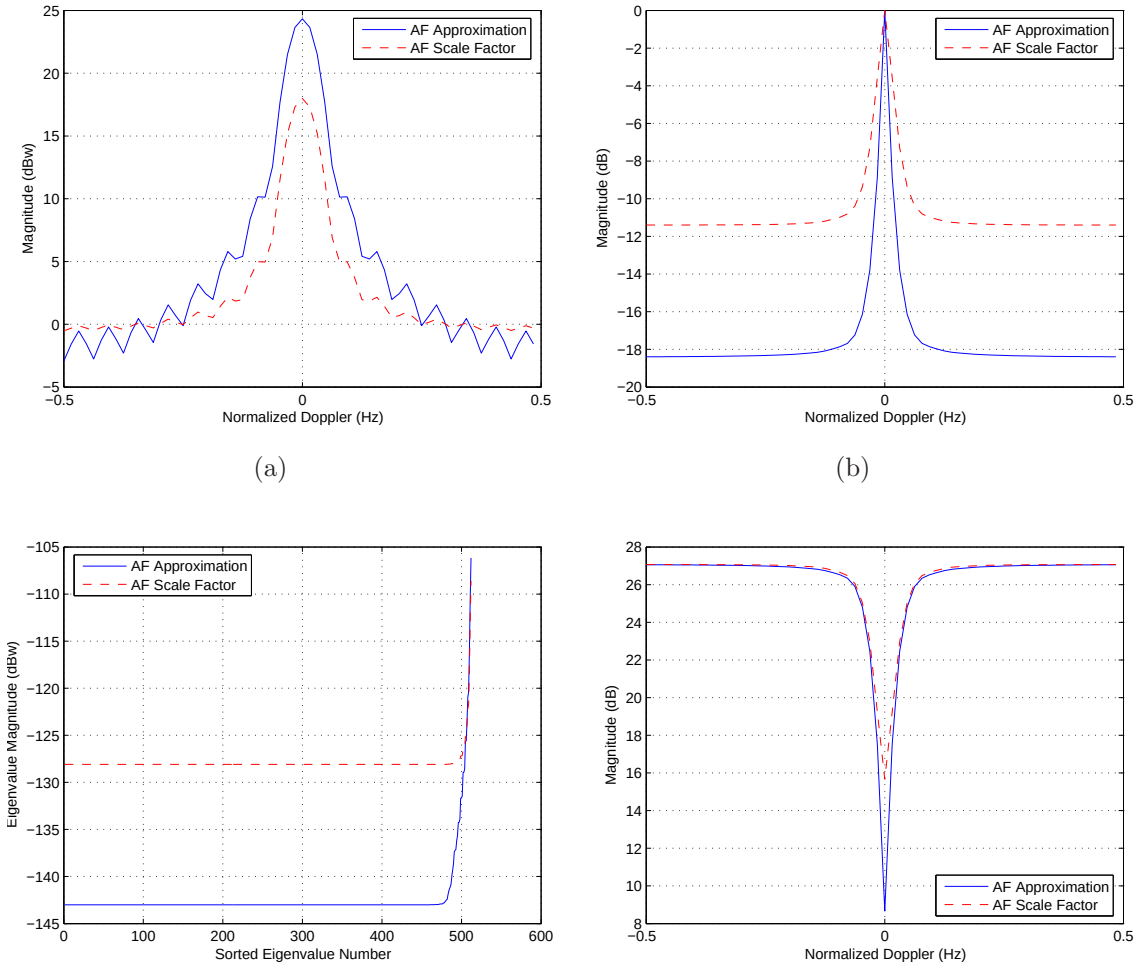

Figure 4.14: Second Gold Coded Pulse
(a) Signal match describing the clutter spectrum.
(b) MVE describing the resolution capability utilizing this waveform.
(c) Eigenvalue decomposition illustrating the rank of the clutter spectrum and the overall difficulty of the problem.
(d) Output SINR of fully adaptive Space Time Adaptive Processing (STAP) illustrating target detection capability at all normalized Doppler frequencies.

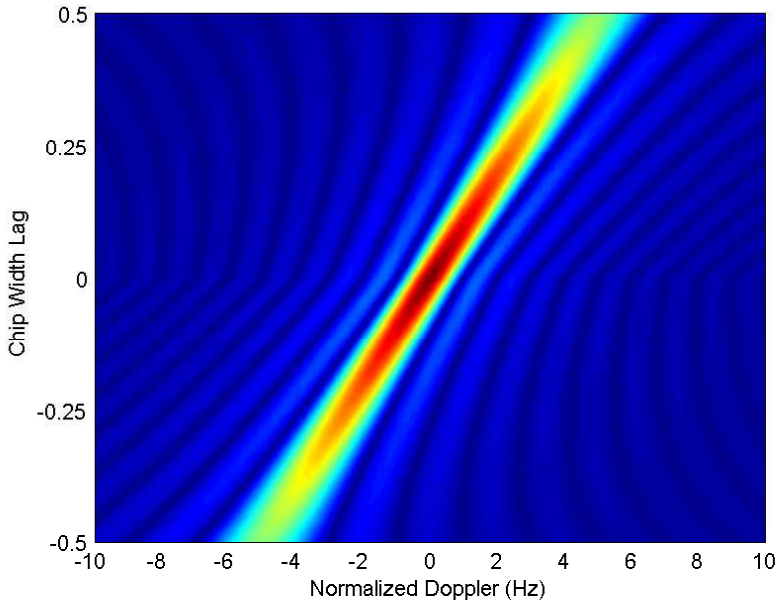

Figure 4.15: The Time Frequency Auto Correlation Function Plot of the Linear Frequency Modulated pulse.

the other waveforms examined. Therefore, the special case for the LFM derived in Chapter 3 is used to model the effects. To ensure that the derived TFACF in chapter is correct, the TFACF of the LFM is required. Figure 4.15 shows the results from the derived TFACF. This figure is what is expected for the TFACF give confidence that the derivation is correct.

The first case examined for the LFM case is the signal match technique as seen in Fig. 4.16 (a). As shown, a 4 dB loss in clutter return power results from implementing the LFM. This clutter spectrum resembles the other clutter spectrum found using the discrete waveforms.

The next step is to evaluate how the resolution is effected using the LFM. Figure 4.16 (b) shows that range resolution is lost by implementing this compressed waveform. Any targets that fall into the main beam maybe lost due to high clutter power.

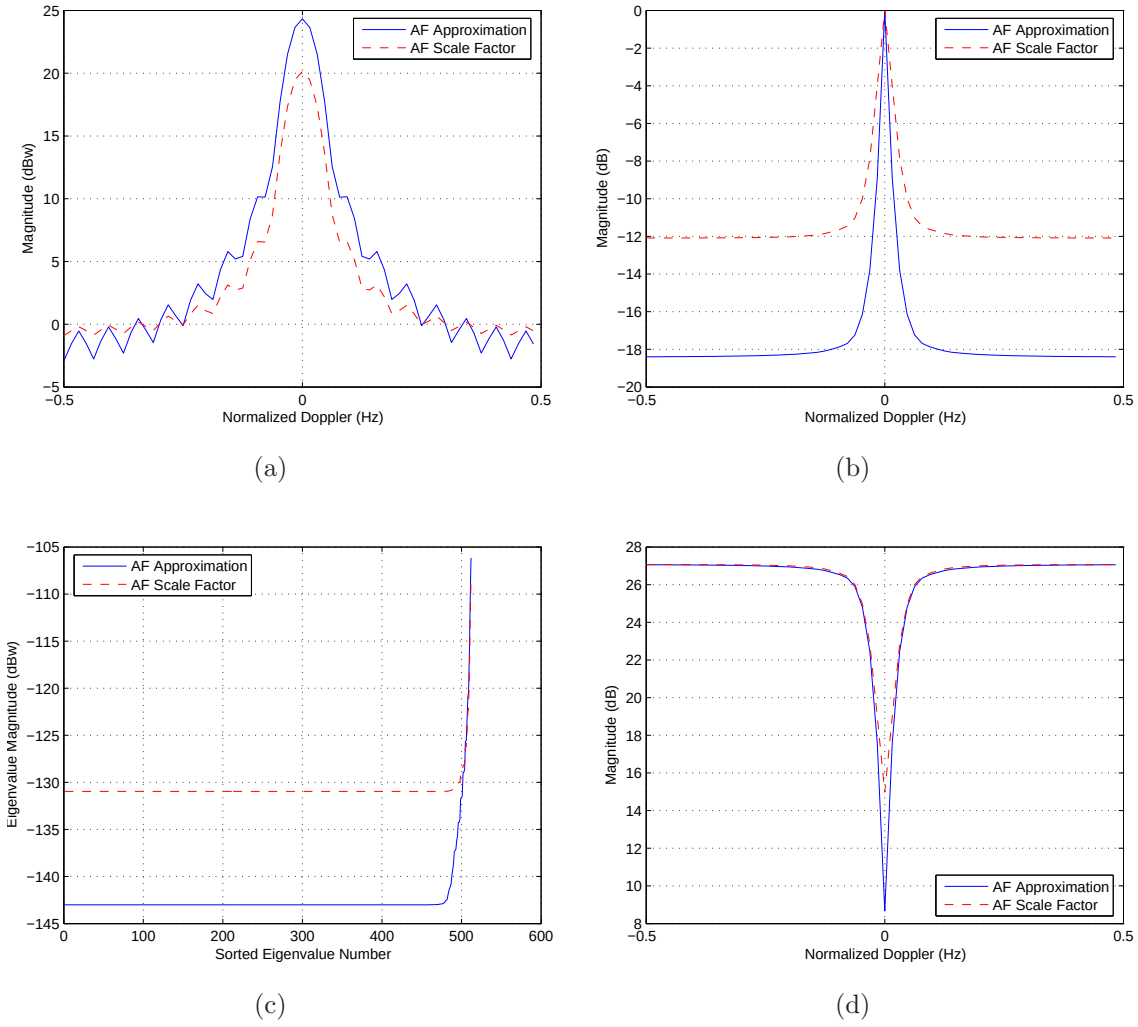

Figure 4.16: Linear Frequency Modulated Coded Pulse
(a) Signal match describing the clutter spectrum.
(b) MVE describing the resolution capability utilizing this waveform.
(c) Eigenvalue decomposition illustrating the rank of the clutter spectrum and the overall difficulty of the problem.
(d) Output SINR of fully adaptive Space Time Adaptive Processing (STAP) illustrating target detection capability at all normalized Doppler frequencies.

The bandwidth for the LFM waveform is calculated differently than that of the discrete waveforms. Bandwidth for a LFM waveform is defined as

$$\mathrm{B}_{\mathrm{lfm}} = f_2 - f_1 \tag{4.24}$$

where f_1 and f_2 is the starting and stopping frequency from the chirped waveform [5]. For this simulation, a bandwidth of 20 $\mathrm{MH_z}$ was used. Since this waveform is smaller than some of the other compression schemes, the thermal noise introduced to the system is smaller. Figure 4.16 (c) shows that the noise floor is at -131 dB. This level allows more clutter returns than the larger compression schemes making for a difficult clutter problem.

The last step is to examine the output SINR of the fully adaptive STAP. This output is shown in Fig. 4.16 (d). A gain of 7 dB is achieved from implementing this LFM waveform. This gain means that the main beam clutter is not as large as it is with the approximation. Therefore, targets are able to be detected with more ease.

The examination of several different waveforms is now complete. Analysis was conducted using four different techniques, signal match, minimum variance estimation, eigenvalue decomposition and output SINR of fully adaptive STAP.

V. Conclusions

The radar model encompasses many different aspects to create an accurate representation of real-world environments. To complete this model, an understanding of how the signal is transmitted and received is paramount. The received signal contains target information. In a perfect world, the power that was transmitted would be the same power received. However, there are outside factors such as thermal noise and ground clutter that effect radar detection capability and need to be accounted for in the model.

Typically, the radar model makes an approximation on processing the received data. This approximation is that there is no Doppler or range shift when matched filtering the received signal with the transmitted signal. This assumption makes the Time Frequency Auto Correlation Function (TFACF) equal one. This research removes that assumption and analyzes the performance effects on the radar model using the TFACF.

After deriving the generic TFACF expression, simulations were run for several different waveforms including a 13-length Barker, 26-length concatenated Barker, two Frank codes (M=5 and M=10), two Gold codes and a Linear Frequency Modulated code. From the results seen in Chapter 4, there were some performance degradations and gains on the radar model. The performance degradation was apparent within the resolution capabilities. Each waveform experienced a loss in resolution which overall effects the radar's ability to distinguish targets located close to each other.

Improvements were noticed within the reduced amount of returned clutter power as well as the difficulty of the clutter problem. All the implemented waveforms reduced the power return from the clutter. This reduction allows for better target detection since the target power has less interference to compete against. Thermal noise plays a major role with in this reduction. The amount of thermal noise allowed is directly proportional to the bandwidth of the pulse. The larger the bandwidth,

the greater effect from thermal noise. This increase in thermal noise dominates the clutter power being returned. Thus, the clutter power is not as effective on the system. This is also seen in the eigenvalue decompositions. The Eigenvalue decomposition provides a metric describing the difficulty of the clutter environment. In all the decomposition plots, the thermal noise floor is raised considerably. This raised effect dominates less clutter return values making the problem less difficult.

Like every radar problem, there are trade-offs. By approximating the TFACF to one, there are performance characteristics that are not accounted for that effect the system. Assuming this approximation, the radar model provides better range resolution than what is actually achievable. However, approximating the TFACF, a worse case scenario is established. This scenario allows for a more difficult clutter power and more main beam clutter power introduced into the model. This introduction hampers target detection capabilities with the radar model. Therefore, a decision must be made when creating the radar model. If accurate resolution is required, the TFACF approximation is not recommended. However, if the model is created to overcome clutter power, then the approximation is fine due to the over estimation of actual clutter power.

By assuming the TFACF is approximately one, important information is lost. Depending on the waveform and its bandwidth, the picture of the interference environment could be distorted. There is some error within the current assumption but not enough to include in the radar model.

Future work with this topic could include removing the limitation of the pulse only mismatching by less than one half a chip or how multiple time around pulses could effect the model. Another idea is to integrate a barrage noise jammer into the model to see the effects, if any, the jammer has on this model.

Appendix A. Matlab Code

This appendix contains the Matlab® code used to model both the conventional and the scaled Time Frequency Auto Correlation Function (TFACF) radar models.

A.1 TFACF Function (Discrete Case)

Listing A.1: A function calculating the discrete case of the TFACF. (appendix1/tfacf.m)

```
%============================================================
% Created By: Capt Gregg Izdepski
% Date: 21 Mar 05
%
%This function calculates the discrete form of the Time Frequency
%Auto Correlation Function.  There is the capability to implement
%seven different pulse compression waveforms within the code.
%Simply remove the comments of the desired code and run the
%program.  The variable 'waveform' is passed for the file name
%while saving the plots.  'Tc' is passed to help calculate the
%bandwidth. 'chips' contains the value of the TFACF.
%============================================================


function [chips,Tc,waveform]=TFACF(tau,f_t,numSubCells,q)

clear chip;
% %============================================================
% %simple rect pulse
% psi=zeros(1,1);
% waveform='rect';

% %============================================================
% %13-length Barker Code
psi=[zeros(5,1); pi; pi; 0; 0; pi; 0; pi; 0];
waveform='Barker';
% psi=[psi; flipud(psi)];
% waveform='Con_Barker';


% %============================================================
% %Frank Code
% M=10;
%
```

```
% % This is for values in degrees
% x=linspace(0,360-360/M,M);
% y=[0:1:M-1]';
% matrix=y*x;
% max_value=round((max(max(matrix)))/360);
%
% % This is for values in radians
% x=linspace(0,2*pi-2*pi/M,M); %for values in radians
% y=[0:1:M-1]';
% matrix=y*x;
% max_value=round((max(max(matrix)))/2/pi);
%
% % Creating the matrix
% for p=1:max_value
%     for k=1:M
%         temp_matrix=[matrix(k,:)];
%         for m=1:M
%
% %This is for values in degrees
%
%             if temp_matrix(:,m)>=360
%                 temp_matrix(:,m)=temp_matrix(:,m)-360;
%             else
%                 temp_matrix(:,m)=temp_matrix(:,m);
%             end
%
% %This is for values in radians
%
%             if temp_matrix(:,m)>=2*pi
%                 temp_matrix(:,m)=temp_matrix(:,m)-2*pi;
%             else
%                 temp_matrix(:,m)=temp_matrix(:,m);
%             end
%         end
%         interim(k,:)=temp_matrix;
%     end
%     matrix=interim;
% end

% psi=matrix(:);
% waveform='frank_10';    %check that the # equals M


%=============================================================
%Gold Code
% code_1=[0001101111011010001111110100000]'*pi;
% code_2=[0101100101100001001000000111010]'*pi;
%
% psi=code_1;           %change the _# to select code #1 or #2
% waveform='gold_1';    %check that numbers are matching

```

```
P=length(psi);      % # of chips
Tc=tau/P;           % Chip time

%=============================================================
%subdivsions within the ring

% matching the document...tau_prime is the delay, tau-T_R
tau_prime=linspace(-Tc/2,Tc/2,numSubCells);
tau_prime=tau_prime(q);

%=============================================================
%calculating the TFACF
chips=zeros(length(tau_prime),1);

% The less than case expression
if tau_prime < 0
    for p=0:P-1
        if p~=P-1
            chip(p+1)=1/P/Tc*( ...
                (Tc+tau_prime)*...
                exp(j*pi*f_t*((2*p+1)*Tc+tau_prime))*...
                sinc(f_t*(Tc+tau_prime))-...
                exp(j*psi(p+1)-j*psi(p+2))*tau_prime*...
                exp(j*pi*f_t*(2*(p+1)*Tc+tau_prime))*...
                sinc(f_t*tau_prime));
        else
            chip(p+1)=1/P/Tc*( ...
                (Tc+tau_prime)*...
                exp(j*pi*f_t*(Tc*(2*p+1)+tau_prime))*...
                sinc(f_t*(Tc+tau_prime)));
        end
    end

    chips = sum(sum(chip));
    clear chip;

% The greater than case expression
elseif tau_prime > 0
    for p=0:P-1
        if p==0
            chip(p+1)=1/P/Tc*( ...
                (Tc-tau_prime)*...
                exp(j*pi*f_t*((2*p+1)*Tc+tau_prime))*...
                sinc(f_t*(Tc-tau_prime)));
        else
            chip(p+1)=1/P/Tc*( ...
                (Tc-tau_prime)*...
                exp(j*pi*f_t*((2*p+1)*Tc+tau_prime))*...
                sinc(f_t*(Tc-tau_prime))+...
                exp(j*(psi(p+1)-psi(p)))*tau_prime*...
                exp(j*pi*f_t*(2*p*Tc + tau_prime))*...
```

```
                    sinc(f_t*tau_prime));
            end
        end

        chips = sum(sum(chip));
        clear chip;

    else

    %The equal to case expression
        chips = sinc(f_t*P*Tc);
    end
```

A.2 TFACF Function (LFM)

Listing A.2: A function calculating the continuous LFM case of the TFACF. (appendix1/TfacfLfm.m)

```
%================================================================
% Created By: Capt Gregg Izdepski
% Date: 21 Mar 05
%
%This function calculates the Time Frequency Auto Correlation
%Function of the continuous LFM waveform.  It returns the TFACF
%value in 'chips' and 'waveform' is the root filename for saving
%the analysis plots.
%================================================================

function [chips,b,waveform]=TFACF_lfm(tau,f_t,numSubCells,q)

waveform='lfm';

b=-5e13;    %chirp rate

tau_prime=linspace(-tau/2,tau/2,numSubCells);
tau_prime=tau_prime(q);
chips=zeros(length(tau_prime),1);

% The less than expression
if tau_prime < 0
    chip=(1/tau)*exp(-j*2*pi*b*tau_prime^2)*...
        exp(j*pi*(2*b*tau_prime+f_t)*(tau+tau_prime))*...
        (tau+tau_prime)*...
        sinc((2*b*tau_prime+f_t)*(tau+tau_prime));

    chips=sum(sum(chip));
    clear chip;

%The greater than expression
```

```
elseif tau_prime > 0
    chip=(1/tau)*exp(-j*2*pi*b*tau_prime^2)*...
        exp(j*2*pi*(2*b*tau_prime+f_t)*tau_prime)*...
        exp(j*pi*(2*b*tau_prime+f_t)*(tau-tau_prime))*...
        (tau-tau_prime)*...
        sinc((2*b*tau_prime+f_t)*(tau-tau_prime));

    chips=sum(sum(chip));
    clear chip;

%The equal to expression
else
    chips = sinc(f_t*tau);
end
```

A.3 Antenna Pattern Function

Listing A.3: A function calculating the necessary antenna pattern for weighting the clutter returns.
(appendix1/antenna.m)

```
%=============================================================
% Created by: Capt Gregg Izdepski
% Date: 21 Mar 05
%
% This function builds the transmitted antenna pattern.  The
% pattern built here is used to scale the clutter returns.
%=============================================================

function [g, g_log, w_af]=antenna(theta, phi, N, P, fo)

%Global Parameters
c=3e8;           % speed of propogation
lambda=c/fo;     % wavelength

%backlobe attenuation factor
dB=-30;              % dB attenuation factor
back=10^(dB/10);     % backlobe weighting factor

%building the element pattern
g=(abs(cos(theta)*cos(phi'))).^2;
a=[find(phi <= -90*pi/180); find(phi >= 90*pi/180)];
temp=g(:,a)*back;
g(:,a)=temp;

g_log=10*log10(abs(g/max(max(g))));        %normalizing g

%raising the floor to -50 dB
g_log=(g_log > -50).*g_log + (g_log <= -50)*(-50);
```

```
%array factor
delta_z=lambda/2;
delta_x=lambda/2;
var_x=(pi*delta_x/lambda);  %dx portion of array factor
var_z=(pi*delta_z/lambda);  %dz portion of array factor

%Building the Array Factor
for i=1:length(theta)
    for h=1:length(phi)
        w_af(i,h)=exp(j*var_z*(P-1).*sin(theta(i))).*...
            exp(j*var_x*(N-1).*cos(theta(i)).*sin(phi(h)))...
            .*sin(var_z*P.*sin(theta(i))).*sin(var_x*N.*...
            cos(theta(i)).*sin(phi(h))./...
            (sin(var_z.*sin(theta(i))).*sin(var_x.*...
            cos(theta(i)).*sin(phi(h))));
    end
end

%Array Factor special cases
w_zeros=N*P;
w_theta=N*exp(j*var_z*(P-1).*sin(theta)).*...
    ((sin(var_z*P.*sin(theta))./(sin(var_z.*sin(theta))));
w_phi=P*exp(j*var_x*(N-1).*sin(phi')).*...
    ((sin(var_x*N.*sin(phi'))./(sin(var_x.*sin(phi')))));

%the complete array factor matrix (accounting for special cases)
if ~isempty(find(phi==0))
    w_af(:,find (phi==0))=w_theta;
end

if ~isempty(find(theta==0))
    w_af(find(theta==0),:)=w_phi;
end

if ~isempty ([find(theta==0) find(phi==0)])
    w_af(find(theta==0),find(phi==0))=w_zeros;
end

return
```

A.4 Conventional Clutter Model Function

Listing A.4: A function calculating the conventional clutter model. (appendix1/clutter.m)

```
%=============================================================
% Created by: Capt Gregg Izdepski
% Date: 21 Mar 05
```

```
%
%This function calculates the clutter covariance matrix for the
%conventional model.  Within this model, the Time Frequency Auto
%Correlation Function is assumed to equal one.
%=============================================================

function [R_clut]=clutter(M,N,P,fo,prf,alt,tau,R,B,delta_x...
    ,delta_z,Pt,elem_gain,Ls)

%=============================================================
%Known parameters
r_earth=6371e3;     %radius of the earth in m
c=3e8;              %propogation speed
gamma_dB=-3;        %clutter gamma in dB
Nc=361;             %# of clutter patches around the clutter ring
To=290;             %standard temp (K)
k=1.380685e-23;     %Boltzman constant

%=============================================================
%Calculated parameters
Tr=1/prf;                   %PRI
K=floor(Tr/tau);            %number of range cells
a_earth=4*r_earth/3;        %effective radius of the earth
gamma=10^(gamma_dB/10);     %gamma in watts
velocity=delta_x/(2*Tr);    %a/c velocity (m/s)
lambda=c/fo;                %lambda in m
No=k*To;                    %standard noise No
sigma=B*No;                 %sigma for the noise

%=============================================================
%Clutter Covariance Matrix

Ru=c/(prf*2);                   %unambigous range
Rh=sqrt(alt^2+2*alt*a_earth);   %horizontal range

%determining Rc range for each bin
bin_time=(Tr-tau)/K;
range=(0:c*bin_time/2:c*K*bin_time/2-c*bin_time/2);

%locating the range bin for the range
bin_desired=find(abs(range-R)==min(abs(range-R)));

Rclut=range(bin_desired);       %cycling current Rc's
Nr=Rh/Ru;                       %calculating Nr

if Rclut*Nr <= Rh
    Nr=ceil (Nr);
else
    Nr=floor (Nr);
end
```

```
Ri=(0:Nr-1)*Ru + Rclut;        %ambigous range cells
del_r=c/(2*B);                 %range resolution

%azimuth clutter angles
del_phi=2*pi/Nc;
phi_clut=(-pi:del_phi:pi-del_phi)';

%elevation clutter angles
theta_clut=-asin(((Ri.^2)+alt*(alt+2*a_earth))./...
    (2*Ri.*(alt+a_earth)))';

%creating the antenna pattern (antenna fn)
[g, g_log, w_af]=antenna(theta_clut, phi_clut, N, P, fo);

%grazing angle
psi_clut=-asin(((Ri.^2)-alt*(alt+2*a_earth))./(2*Ri.*a_earth));

%intializing the covariance matrix
R_c=zeros(M*N*P,M*N*P);

vis=waitbar(0,'Calculating Rings...');
for i=1:Nr
    if Ri(i)>alt;

        %ground reflectivity
        sigma_c=gamma*sin(psi_clut(i)).*Ri(i).*del_phi*...
            del_r.*sec(psi_clut(i));

        for k=1:length(phi_clut)

            var_x=(delta_x*sin(phi_clut(k))*...
                cos(theta_clut(i)))/lambda;
            var_z=(delta_z*sin(theta_clut(i)))/lambda;
            w_bar=(2*velocity*cos(theta_clut(i))*...
                sin(phi_clut(k))/lambda)*Tr;

            steer_a=exp(j*2*pi*[0:N-1]'*var_x);
            steer_b=exp(j*2*pi*[0:M-1]'*w_bar);
            steer_e=exp(j*2*pi*[0:P-1]'*var_z);

            %the steering vector
            v=kron(steer_e,kron(steer_b,steer_a));

            G=abs(w_af(i,k).^2)*g(i,k);

            %CNR per patch
            xsi_c(i,k)=(Pt*G*g(i,k)*elem_gain*(lambda^2)*...
                sigma_c)/(((4*pi)^3)*No*B*Ls*Ri(i)^4);

            %building the covariance matrix
            R_c=R_c+sigma*xsi_c(i,k)*v*v';
```

```
            end
        end
        waitbar(i/Nr,vis)
    end
close (vis)
R_clut=R_c;
```

A.5 Scaled Clutter Model Function

Listing A.5: A function calculating the TFACF scaled clutter model. (appendix1/ClutterDop.m)

```
%=============================================================
% Created by: Capt Gregg Izdepski
% Date: 21 Mar 05
%
%This function calculates the clutter covariance matrix for the
%model scaled by the Time Frequency Auto Correlation Function
%(TFACF).  The code in this model is very similar to that of the
%conventional clutter model.  The difference is noted when
%finding the steering vector b.  Steering vector b is scaled by
%the appropriate TFACF value.
%=============================================================
function [R_clut_dop, sigma, waveform]=clutter_dop(M,N,P,fo,prf...
    ,...
     alt,tau,R,B,delta_x,delta_z,Pt,elem_gain,Ls,numSubCells)

%=============================================================
%Known parameters
r_earth=6371e3;     %radius of the earth in m
c=3e8;                          %progation speed
gamma_dB=-3;        %clutter gamma in dB
Nc=361;             %# of clutter patches around the clutter ring
To=290;             %standard temp (K)
k=1.380685e-23;     %Boltzman constant


%=============================================================
%Calculate parameters
Tr=1/prf;                   %PRI
K=floor(Tr/tau);            %number of range cells
a_earth=4*r_earth/3;        %effective radius of the earth
gamma=10^(gamma_dB/10);     %gamma in watts
velocity=delta_x/(2*Tr);    %a/c velocity (m/s)
lambda=c/fo;                %lambda in m
No=k*To;                    %standard noise No
sigma=B*No;                 %sigma for the noise

%=============================================================
```

```
%Clutter Covariance Matrix

Ru=c/(prf*2);                    %unambigous range
Rh=sqrt(alt^2+2*alt*a_earth);    %horizontal range

%determining Rc range for each bin
bin_time=(Tr-tau)/K;
range=(0:c*bin_time/2:c*K*bin_time/2-c*bin_time/2);

%locating the range bin for the range
bin_desired=find(abs(range-R)==min(abs(range-R)));

Rclut=range(bin_desired);        %cycling current Rc's
Nr=Rh/Ru;    %calculating Nr
% Nr=1;

if Rclut*Nr <= Rh
    Nr=ceil (Nr);
else
    Nr=floor (Nr);
end


Ri=(0:Nr-1)*Ru + Rclut;        %ambigous range cells
del_r=c/(2*B);                 %range resolution

%azimuth clutter angles
del_phi=2*pi/Nc;
phi_clut=(-pi:del_phi:pi-del_phi)';

%intializing the covariance matrix
R_c=zeros(M*N*P,M*N*P);

%Dividing each main range cell into subcells
r_sub=linspace(0,del_r,numSubCells);

vis=waitbar(0,'Calculating Rings...');
for i=1:Nr
    if Ri(i)>alt;
        disp(['Range ring center is ',num2str(Ri(i)/1e3),' km']);

        vis_a=waitbar(0,'Calculating Subrings...');
        for q=0:numSubCells-1

            %fining range to each smaller cell
            Rq=Ri(i)-del_r/2+r_sub(q+1);

            %grazing angle
            psi_clut=-asin(((Rq^2)-alt*(alt+2*a_earth))/...
                (2*Rq*a_earth));
```

```
            %ground reflectivity
            sigma_clut=gamma*sin(psi_clut)*Rq*del_phi*...
90              mean(diff(r_sub))*sec(psi_clut);

            %elevation clutter angles
            theta_clut=-asin(((Rq^2)+alt*(alt+2*a_earth))/...
                (2*Rq*(alt+a_earth)));
95
            var_z=(delta_z*sin(theta_clut))/lambda;
            steer_e=exp(j*2*pi*[0:P-1]'*var_z);

            for k=1:length(phi_clut)
100             %creating the antenna pattern (antenna fn)
                [g,g_log,w_af]=antenna(theta_clut,phi_clut(k),...
                    N,P,fo);

                var_x=(delta_x*sin(phi_clut(k))*...
105                 cos(theta_clut))/lambda;
                w_bar=(2*velocity*cos(theta_clut)*...
                    sin(phi_clut(k))/lambda)*Tr;

%These next two lines determine which TFACF is called.  One of
110 %these two should be commented out while running sims.
%Otherwise, only the LFM TFACF will be return (since it is last)

                %This is for the discrete TFACF
                [chips,Tc,waveform]=TFACF(tau,w_bar/Tr,...
115                 numSubCells,(q+1));
                B=1/Tc;     %calculates the bandwidth

                %This is for the LFM TFACF
%               [chips, b, waveform]=TfacfLfm(tau,w_bar/Tr,...
120 %                   numSubCells,(q+1));
%               B=b*tau;    %LFM bandwidth

                sigma=B*No;     %calculating the noise power

125             steer_a=exp(j*2*pi*[0:N-1]'*var_x);
                steer_b=exp(j*2*pi*[0:M-1]'*w_bar)*chips;

                v_dop=kron(steer_e,(kron(steer_b,steer_a)));

130             G=abs(w_af^2)*g;

                xsi_c=(Pt*G*g*elem_gain*(lambda^2)*sigma_clut)...
                   /...
                    (((4*pi)^3)*No*B*Ls*Rq^4);

135             R_c=R_c+sigma*xsi_c*v_dop*v_dop';
            end
```

```
            waitbar((q+1)/numSubCells,vis_a);
        end
        close (vis_a);
    end
    waitbar(i/Nr,vis);

end
close (vis);
R_clut_dop=R_c;
```

A.6 Overall Model

Listing A.6: The overall model incorporating all functions. Analysis is completed here allowing for analysis.
(appendix1/ModelClutter.m)

```
%============================================================
% Created by: Capt Gregg Izdepski
% Date: 21 Mar 05
%
%This code incorporates all functions to create the two different
%radar models, conventional and scaled.  This code should remain
%unchanged since all parameters are changed within the functions.
%The only changes are title descriptions, if desired.  The plots
%are directly saved to the current file directory
%(both *.*eps and *.*png).
%============================================================
close all; clear all; clc; format compact;

tic;
%============================================================
%Global Parameters
M=16;                  %pulses
N=16;                  %# of azimuth channels
P=2;                  %# of elevation channels
fo=1.24e9;            %transmitted frequency (GHz)
prf=1984;             %pulse repetition frequency
tau=0.8e-6;           %pulse width
Pt=1.5e3;             %power transmitted (kW)
B=1/tau;              %bw in Hz
Fn_dB=3;              %noise figure in dB
alt=9e3;              %a/c altitude (m)
R=66e3;               %Range to target in m
delta_x=0.10922;      %azimuth channel spacing (m)
delta_z=0.140716;     %elevation channel spacing (m)
Ls_dB=3;              %system loss in dB
elem_gain_dB=0;       %element gain in dB
To=290;               %standard temp (K)
k=1.380685e-23;       %Boltzman constant
```

```
c=3e8;                %propogation speed
velocity=90;          %a/c velocity (m/s)
numSubCells=101;      %# of smaller clutter rings in each main ring

%=============================================================
%calculated constants
Ls=10^(Ls_dB/10);                %system loss in watts
elem_gain=10^(elem_gain_dB/10); %element gain in watts
No=k*To;                         %standard noise No
sigma=B*No;                      %sigma for the noise
lambda=c/fo;                     %lambda (m)

%=============================================================
%Clutter Covariance Matricies

%Clutter assuming no doppler tolerance
[R_clut]=clutter(M,N,P,fo,prf,alt,tau,R,B,delta_x,delta_z,Pt,...
    elem_gain,Ls);

%Clutter w/ doppler effect
[R_clut_dop,sigma_dop,waveform]=ClutterDop(M,N,P,fo,prf,alt,...
    tau,R,B,delta_x,delta_z,Pt,elem_gain,Ls,numSubCells);

%=============================================================
%Thermal Noise Block Matrix

R_noise=sigma*eye(M*N*P);

%calculating new noise matrix for implement waveform
sigma_dop=B_dop*No;
R_noise_dop=sigma_dop*eye(M*N*P);

%=============================================================
%Total R matrix (including clutter and thermal noise)

R_tot=R_clut+R_noise;                %conventional data
R_tot_dop=R_clut_dop+R_noise_dop;    %scaled data

%=============================================================
%creating the steering vector

var_x=(delta_x*sin(0)*cos(0))/lambda;
var_z=(delta_z*sin(0))/lambda;
pad=2^(log2(M)+2);
w_bar=linspace(-0.5,0.5-1/pad,pad)';

steer_a=exp(j*2*pi*[0:N-1]'*var_x);
steer_b=exp(j*2*pi*[0:M-1]'*w_bar');
steer_e=exp(j*2*pi*[0:P-1]'*var_z);

v=kron(steer_e,kron(steer_b,steer_a));
```

```
85
   %=================================================================
   %Spectra Analysis

   %************************************
90 %Signal Match (SM)
   P_sm=diag(v'*R_tot*v)./diag(v'*v*R_tot(1,1));
   P_sm_dop=diag(v'*R_tot_dop*v)./diag(v'*v*R_tot_dop(1,1));

   figure;
95 plot (w_bar,10*log10(abs(P_sm)),w_bar,10*log10(abs(P_sm_dop))...
       ,'r--');grid on;
   xlabel('Normalized Doppler (Hz)');
   ylabel('Magnitude (dBw)');
   legend ('AF Approximation','AF Scale Factor');
100 % title ('Signal Match (SM) Method');

   %saving the SM plotted results
   print('-depsc',[waveform '_sm_dop.eps']);
   print('-dpng',[waveform '_sm_dop.png']);
105
   %************************************
   %Minimum Variance Estimator (MVE)
   P_mve=1./diag(v'*(R_tot\v));
   P_mve_dop=1./diag(v'*(R_tot_dop\v));
110
   figure;
   plot(w_bar,10*log10(abs(P_mve)/max(abs(P_mve))),w_bar,...
       10*log10(abs(P_mve_dop)/max(abs(P_mve_dop))),'r--');grid on;
   xlabel('Normalized Doppler (Hz)');
115 ylabel('Magnitude (dB)');
   legend ('AF Approximation','AF Scale Factor');
   % title ('Minimum Variance Estimator (MVE) Method');

   %saving the MVE plotted results
120 print('-depsc',[waveform '_mv.eps']);
   print('-dpng',[waveform '_mv.png']);

   %************************************
   %Eigenvalue
125 Eig_R_tot=eig(R_tot);
   Eig_R_tot_dop=eig(R_tot_dop);

   figure;
   plot(1:length(Eig_R_tot),10*log10(abs(sort(Eig_R_tot))), ...
130     1:length(Eig_R_tot_dop),10*log10(abs(sort(Eig_R_tot_dop)))...
       ,'r--');grid on;
   xlabel('Sorted Eigenvalue Number');
   ylabel('Eigenvalue Magnitude (dBw)');
   legend('AF Approximation','AF Scale Factor',2);
135 % title('Eigenvalue Comparison');
```

```
%saving the Eigenvalue plotted results
print('-depsc',[waveform '_eig.eps']);
print('-dpng',[waveform '_eig.png']);

%************************************
%Optimum SINR
SINR=diag(sigma*v'*(R_tot\v));
SINR_dop=diag(sigma_dop*v'*(R_tot_dop\v));

figure;
plot(w_bar,10*log10(abs(SINR)),w_bar,10*log10(abs(SINR_dop))...
    ,'r--');grid on;
xlabel('Normalized Doppler (Hz)');
ylabel('Magnitude (dB)');
legend('AF Approximation','AF Scale Factor',4);
% title('Output SINR for a Fully Adaptive STAP Process');

%saving the SINR plotted results
print('-depsc',[waveform '_sinr.eps']);
print('-dpng',[waveform '_sinr.png']);

time=toc/60
```

Bibliography

1. Hale, Todd B. *Airborne radar interference suppression using adaptive three-dimensional techniques.* Master's thesis, Graduate School of Engineering, Air Force Institute of Technology (AETC), Wright-Patterson AFB OH, December 2002. AFIT/DS/ENG/02-02.

2. Hale, Todd B. "Class Notes", August 2004. EENG 678 Adaptive Interference Suppression for Radar.

3. Hale, Todd B., Michael A. Temple, and Benjamin L. Crossley. "Ambiguity Analysis for Pulse Compression Radar Using Gold Code Sequences". *Proceedings of the 1998 IEEE National Radar Conference.* May 1998.

4. Klemm, Richard. *Principles of Space-Time Adaptive Processing.* The Institution of Electrical Engineers, London, United Kingdom, 2002.

5. Skolnik, Merrill. *Introduction to Radar Systems, Third Edition.* The McGraw-Hill Companies, Inc., New York, New York 10020, 2001.

6. Stremler, Ferrel G. *Introduction to Communication Systems, 3rd edition.* Addison Wesley, New York, 1992.

7. Ward, James. *Space-Time Adaptive Processing for Airborne Radar.* Contract F19628-95-C-0002, Lincoln Laboratory, Massachusetts Institute of Technology, Lexington, Massachusetts, December 1994.

REPORT DOCUMENTATION PAGE

Form Approved
OMB No. 0704–0188

1. REPORT DATE *(DD–MM–YYYY)*	2. REPORT TYPE	3. DATES COVERED *(From — To)*
21–03–2005	Master's Thesis	Sept 2003 — Mar 2005

4. TITLE AND SUBTITLE

An Examination of
Range and Doppler Mismatch
and their Effects on Radar Modeling

5a. CONTRACT NUMBER

5b. GRANT NUMBER

5c. PROGRAM ELEMENT NUMBER

6. AUTHOR(S)

Gregory L Izdepski, Capt, USAF

5d. PROJECT NUMBER

5e. TASK NUMBER

5f. WORK UNIT NUMBER

7. PERFORMING ORGANIZATION NAME(S) AND ADDRESS(ES)

Air Force Institute of Technology
Graduate School of Engineering and Management
2950 Hobson Way, Bldg 641
WPAFB OH 45433-7765

8. PERFORMING ORGANIZATION REPORT NUMBER

AFIT/GE/ENG/05-07

9. SPONSORING / MONITORING AGENCY NAME(S) AND ADDRESS(ES)

Dr. Michael Wicks
AFRL/SNRT
26 Electronic Parkway
Rome Air Force Base, NY 13441-4514
michael.wicks@rl.af.mil
DSN 587-2556

10. SPONSOR/MONITOR'S ACRONYM(S)

11. SPONSOR/MONITOR'S REPORT NUMBER(S)

12. DISTRIBUTION / AVAILABILITY STATEMENT

Approval for public release; distribution is unlimited.

13. SUPPLEMENTARY NOTES

14. ABSTRACT

A commonly accepted airborne phased array radar model simplifies the analytical derivation by assuming a waveform is perfectly matched in range and Doppler shift. This assumption means the matched filter output is effectively constant for all possible received scatterer Doppler and range mismatches, greatly simplifying the analytical development from that point forward. This research removes the matched Doppler and range assumption and examines the effects of several common waveforms on the model's fidelity along with the associated impact on radar performance, both non-adaptive and adaptive. Analysis is completed using power spectral density comparisons and the fully adaptive output signal to interference plus noise ratio comparison. Results indicate that the model's fidelity is impacted little by the Time Frequency Auto Correlation Function. However, change in bandwidth from the compressed waveforms does impact the model. Increased bandwidth introduces more thermal noise which dominates clutter returns. Therefore, the clutter problem becomes less difficult. The trade-off is a reduction in the resolution capability of the clutter spectrum.

15. SUBJECT TERMS

time frequency auto correlation function, radar model, clutter, waveform diversity

16. SECURITY CLASSIFICATION OF:			17. LIMITATION OF ABSTRACT	18. NUMBER OF PAGES	19a. NAME OF RESPONSIBLE PERSON
a. REPORT	b. ABSTRACT	c. THIS PAGE			Maj Todd B. Hale, PhD
U	U	U	UU	103	19b. TELEPHONE NUMBER *(include area code)* (937) 255–3636, ext 4639,todd.hale@afit.edu